A&A 486, 99–111 (2008)
DOI: 10.1051/0004-6361:20079111

Astronomy & Astrophysics

Long-term variability of the optical spectra of NGC 4151⋆

I. Light curves and flux correlations

A. I. Shapovalova[1], L. Č. Popović[2,3], S. Collin[4], A. N. Burenkov[1], V. H. Chavushyan[5], N. G. Bochkarev[6], E. Benítez[7], D. Dultzin[7], A. Kovačević[8], N. Borisov[1], L. Carrasco[5], J. León-Tavares[5,9], A. Mercado[10], J. R. Valdes[5], V. V. Vlasuyk[1], and V. E. Zhdanova[1]

[1] Special Astrophysical Observatory of the Russian AS, Nizhnij Arkhyz, Karachaevo-Cherkesia 369167, Russia
e-mail: ashap@sao.ru
[2] Astronomical Observatory, Volgina 7, 11160 Belgrade 74, Serbia
[3] Alexander von Humboldt Fellow, presently at Max Planck Institute for Radioastronomy, Bonn, Germany
[4] LUTH, Observatoire de Paris, CNRS, Université Paris Diderot, 5 Place Jules Janssen, 92190 Meudon, France
[5] Instituto Nacional de Astrofísica, Óptica y Electrónica, Apartado Postal 51, CP 72000, Puebla, Pue. México, México
[6] Sternberg Astronomical Institute, Moscow, Russia
[7] Instituto de Astronomía, UNAM, Apartado Postal 70-264, CP 04510, México
[8] Department of Astronomy, Faculty of Mathematics, University of Belgrade, Studentski trg 16, 11000 Belgrade, Serbia
[9] Max-Planck Institute für Radioastronomie, Auf dem Hügel 69, 53121 Bonn, Germany
[10] Universidad Politécnica de Baja California, Av. de la Industria # 291, CP 21010, Mexicali, B.C., México

Received 20 November 2007 / Accepted 7 April 2008

ABSTRACT

Aims. Results of long-term spectral monitoring of the active galactic nucleus of NGC 4151 are presented (11 years, from 1996 to 2006).
Methods. High quality spectra ($S/N > 50$ in the continuum near Hα and Hβ) were obtained in the spectral range ~4000 to 7500 Å, with a resolution between 5 and 15 Å, using the 6-m and the 1-m SAO's telescopes (Russia), the GHAO's 2.1-m telescope (Cananea, México), and the OAN-SPM's 2.1-m telescope (San-Pedro, México). The observed fluxes of the Hα, Hβ, Hγ, and HeIIλ4686 emission lines and of the continuum at the observed wavelength 5117 Å were corrected for the position angle, the seeing, and the aperture effects.
Results. We found that the continuum and line fluxes varied strongly (up to a factor 6) during the monitoring period. The emission was maximum in 1996−1998, and there were two minima in 2001 and in 2005. As a consequence, the spectral type of the nucleus changed from a Sy1.5 in the maximum activity state to a Sy1.8 in the minimum state. The Hα, Hγ, and Heλ4686 fluxes correlated well with the Hβ flux. The line profiles were strongly variable, showing changes of the blue and red asymmetry. The flux ratios of the blue/red wings and of the blue (or red) wing/core of Hα and Hβ varied differently. We considered three characteristic periods during which the Hβ and Hα profiles were similar: 1996−1999, 2000−2001, and 2002−2006. The line-to-continuum flux ratios were different; in particular during the first period (1996–1999), the lines were not correlated with the continuum and saturated at high fluxes. In the second and third periods (2000–2006), where the continuum flux was small, the Hα and Hβ fluxes were well correlated to the continuum flux, meaning that the ionizing continuum was a good extrapolation of the optical continuum. The CCFs are often asymmetrical and the time lags between the lines and the continuum are badly defined, indicating the presence of a complex BLR, with dimensions from 1 to 50 light-days.
Conclusions. We discuss the different responses of Hβ and Hα to the continuum during the monitoring period.

Key words. galaxies: active – galaxies: individual: NGC 4151

1. Introduction

The brightest Seyfert 1.5-type galaxy NGC 4151 has been studied in detail at all wavelengths (e.g. Peterson 1988; and Ulrich 2000). The nucleus of this galaxy shows flux variability in a wide wavelength range, with time scales from a few hours (in the hard X-ray, e.g. Yaqoob et al. 1993) to several months (in the infrared, e.g. Oknyanskij et al. 1999).

In the optical range, the active galactic nucleus (AGN) of this galaxy is also known to display flux variations of the continuum and of the lines up to a factor ten or more (e.g. Peterson 1988; Clavel et al. 1990; Maoz et al. 1991; Shapovalova et al. 1996; Ulrich & Horne 1996; Sergeev et al. 2001; Lyuty 2005). These variations occur on time scales of several days (Maoz et al. 1991).

NGC 4151 has been the subject of echo-mapping observational campaigns. The main aim of AGN monitoring campaigns was to determine the size of the broad line region (BLR) by measuring the time delay between the emission line fluxes, in response to the variations in the continuum flux (see Peterson 1993, for a review). It is interesting that different authors have found different time lags: Antonucci & Cohen (1983) observed NGC 4151 at least once a month from 1980 May through 1981 July. They have also found that the BLR radius was less

⋆ Tables 2–5, 7 and 8 are only available in electronic form at http://www.aanda.org

than 30 lt-days. These observations were used by Peterson & Cota (1988) in combination with their own observations (performed from 1985 to 1986), and they found a BLR radius of 6 ± 4 lt-days. Gaskell & Sparke (1986) applied the cross-correlation method to the ultraviolet data of Ulrich et al. (1984) and to the optical data of Antonucci & Cohen (1983), and they found a BLR size between 2 lt-days (for HeIIλ4686) and 20 lt-days (for Hα).

On the other hand, Maoz et al. (1991) analyzed the observations (optical continuum, Hβ, and Hα) from 67 nights during a 216-day period between December 15, 1987, and July 18, 1988. They found a BLR size of 9 ± 2 lt-days. They also showed that on a time scale of 0 ± 5 days, the wings of Hα and Hβ varied in phase, and they ruled out a purely unidirectional radial motion in the BLR (either inflow or outflow).

A 10-year long monitoring campaign (1988−1998) of the NGC 4151 nucleus was performed with a sampling of 1−2 observations per month, using the CCD spectrograph of the 2.6-m CrAO telescope, which covers the Hα and Hβ spectral range (Malkov et al. 1997; Sergeev et al. 2001). The time delays between the broad lines and the continuum at 5100 Å were 1.5−10 days for the Balmer lines and 0.0−2.6 days for the HeII λ4686 line (Sergeev et al. 2001). Bentz et al. (2006) analyzed the observations performed between February 27 and April 10, 2005. They obtained a time lag for the Hβ line of $6.6^{+1.1}_{-0.8}$ days.

NGC 4151 was also monitored in the UV. Clavel et al. (1990) analyzed the spectra obtained with the IUE satellite during two months from November 29, 1988, to January 30, 1989 (with a ∼4 day sampling time) and found a time lag of 4 ± 3 days between the continuum and the lines CIVλ1549 and Mg IIλ2798. In addition, NGC 4151 was observed with IUE from November 9 to December 15, 1991 (35 days), with a one-day sampling time (see Ulrich & Horne 1996). Ulrich & Horne (1996) found that the time delay in the continuum at 3000 Å with respect to that at 1320 Å was less than one day (i.e. the UV continuum is emitted by a region with a dimension less than one light day). The broad UV emission lines showed large variations that closely followed the continuum ones. For CIVλ1549, the time lag relative to the continuum was 2.4−3.8 days. Ulrich & Horne (1996) also observed deep blue-shifted absorption lines. They are produced by a low-velocity gas that covers the major part of the rapidly varying continuum source and the emission-line regions. This material is moving outwards along the line of sight and may be located anywhere beyond 15 lt-days. Kaspi et al. (1996) observed NGC 4151 during two months in 1993, with a time resolution of about one day. They found no evidence of any time lag between the optical and UV continuum, and a time lag of 0−2 days for Hα and 0−3 days for Hβ. Metzroth et al. (2006) re-analyzed the IUE spectra of NGC 4151 obtained in 1988 (Clavel et al. 1990) and in 1991 (Ulrich & Horne 1996), using the New Spectral Image Processing System (NEWSIPS). This allowed the photometric precision to be improved and the S/N ratio to be increased by 10%−50%. They found that the time lags of the revised responses to changes of the continuum were ∼3−7 days for CIVλ1549, HeIIλ1640, CIII]λ1909, and MgIIλ2798.

The results mentioned above indicate that the dimension of the BLR varies among the emission lines (radial stratification) and is changing with time. Contradictory results have been obtained, even for the same species, after using the modified processing system and re-analyzing old data (for instance, Antonucci & Cohen 1983; Gaskell & Sparke 1986; Peterson & Cota 1988; Ulrich & Horne 1996; Metzroth et al. 2006). Inconsistent time lags from different monitoring campaigns might be caused by the short duration of the campaigns, but might also indicate real changes in the BLR size and geometry; for example Lyuty (2005) analyzed photometric observations performed during more than 30 years and concluded that the NGC 4151 nucleus goes through different levels of activity. They could be related to a total destruction of the accretion disk (AD) that took place in cycle A (from 1968 to 1984) and to the formation of a new AD in cycle B (from 1989 to 1996). Nevertheless, most UV and optical monitoring campaigns confirmed that the BLR is small and is radially stratified.

Unfortunately, spectral optical monitoring of NGC 4151 were mostly carried out during periods that were too short (less than one year), to trace real changes in the BLR structure. More than 10 years of spectral monitoring is needed to study the evolution of the BLR. Such observations have been made since 1986 in CrAO (Malkov et al. 1997; Sergeev et al. 2001) and SAO RAS (Bochkarev et al. 1988, 1991; Shapovalova et al. 1996; Nazarova et al. 1998).

In this paper we present the analysis of the spectral monitoring of NGC 4151 which covers a 11-year period from 1996 to 2006. The paper is organized as follows. In Sect. 2 the observations, data reduction and calibration are explained. In Sect. 3 we study the correlations between the continuum, the Balmer (Hα, Hβ, Hγ), and the HeIIλ4686 fluxes for both the whole lines and the line wings. In Sect. 4 we discuss different possible interpretations, and the results are summarized in Sect. 5.

2. Observations and data reduction

2.1. Optical spectroscopy

Spectroscopic observations of NGC 4151 were carried out between January 11, 1996 (Julian Date = JD 2 450 094) and April 20, 2006 (JD 2 453 846), thus covering a period of more than 10 years. In total 180 blue and 137 red spectra were taken during 220 nights (i) with the 6-m and 1-m telescopes of SAO, Russia (1996−2006); (ii) with the 2.1-m telescope of the Guillermo Haro Astrophysical Observatory (GHAO) at Cananea, Sonora, México (1998−2006); and (iii) with the 2.1-m telescope of the Observatorio Astronómico Nacinal at San Pedro Martir (OAN-SMP), Baja California, México (2005−2006). The spectra were obtained with a long-slit spectrograph equipped with CCDs. The typical wavelength range was 4000−7500 Å, the spectral resolution was R = 5−15 Å, and the S/N ratio was >50 in the continuum near Hα and Hβ. Note that from 2004 to 2006, the spectral observations with the GHAO's 2.1-m telescope were carried out with two variants of the equipment: 1) with a grism of 150 l/mm (a low dispersion of R = 15 Å, like the observations of 1998−2003); 2) with a grism of 300 l/mm (a moderate dispersion of R = 7.5 Å). As a rule, the observations were performed with the moderate dispersion in the blue or red bands during the first night of each set. During the next night, we usually used the low dispersion in the whole range 4000−7500 Å, and the moderate dispersion was used the following night. Since the shape of the continuum of active galaxies practically does not change during adjacent nights, it was easy to link the blue and red bands obtained with the moderate dispersion, using the data obtained for the continuum with the low dispersion in the whole wavelength range. The photometric accuracy is thus considerably improved with respect to a link obtained by overlapping the extremities of the continuum (3−5% instead of 5−10%).

Table 1. Sources of spectroscopic observations: 1 – Observatory; 2 – code assigned to each combination of telescope + equipment used throughout this paper; 3 – telescope aperture and spectrograph; 4 – projected spectrograph entrance apertures (the first number is the slit width, and the second is the slit length); 5 – focus of the telescope.

Observatory	Code	Tel. and equip.	Aperture	Focus
SAO(Russia)	L(N)	6 m+Long slit	2.0×6.0	Nasmith
SAO(Russia)	L(U)	6 m+UAGS	2.0×6.0	Prime
SAO(Russia)	L(S)	6 m+Scorpio	1.0×6.0	Prime
Gullermo Haro(México)	GH	2.1 m+B&C	2.5×6.0	Cassegrain
San–Pedro(México)	S-P	2.1 m+B&C	2.5×6.0	Cassegrain
SAO(Russia)	L1(G)	1 m+GAD	$4.2(8.0) \times 19.8$	Cassegrain
SAO(Russia)	L1(U)	1 m+UAGS+CCD2K	4.0×9.45	Cassegrain

Spectrophotometric standard stars were observed every night. Information on the source of spectroscopic observations is listed in Table 1. Log of the spectroscopic observations is given in Table 2 (available only in electronic form).

The spectrophotometric data reduction was carried out either with the software developed at the SAO RAS by Vlasyuk (1993) or with IRAF for the spectra observed in México. The image reduction process included bias subtraction, flat-field corrections, cosmic ray removal, 2D wavelength linearization, sky spectrum subtraction, addition of the spectra for every night, and relative flux calibration based on standard star observations.

2.2. Absolute calibration and measurements of the spectra

The standard technique of flux calibration spectra (i.e. comparison with stars of known spectral energy distribution) is not precise enough for the study of AGN variability, since even under good photometric conditions, the accuracy of spectrophotometry is not better than 10%. Therefore we used standard stars only for a relative calibration.

For the absolute calibration, the fluxes of the narrow emission lines are adopted for scaling the AGN spectra, because they are known to remain constant on time scales of tens of years (Peterson 1993). We thus assumed that the flux of the [O III]λ 5007 line was constant during the monitoring period. One can indeed check that it did not change between 1980 (Antonucci & Cohen 1983) and 1992 (Malkov et al. 1997). This is due to the fact that the forbidden line emitting region is very extensive (more than a hundred light-years). All blue spectra were thus scaled to the constant flux $F([\mathrm{O\,III}]\lambda\,5007) = 1.14 \times 10^{-11}$ erg s^{-1} cm^{-2} determined by Malkov et al. (1997), and corrected for the position angle (PA), seeing, and aperture effects, as described in Sect. 2.3. The scaling of the blue spectra was performed by using the method of Van Groningen & Wanders (1992) modified by Shapovalova et al. (2004)[1]. This method allowed us to obtain a homogeneous set of spectra with the same wavelength calibration and the same [OIII]λ5007 flux.

The spectra obtained using the GHAO 2.1-m telescope (México) with a resolution of 15 Å contain both the Hα and Hβ regions. These spectra were scaled using the [O III]λ 5007 line. In this case the red region was also automatically scaled by the [O III]λ 5007 flux. However, the accuracy of such a scaling depends strongly on the correct determination of the continuum slope within the whole wavelength range (4000−7500), i.e. on a correct correction for the spectral sensitivity of the equipment, which is determined by a comparison star. If the night of the observation did not have good photometric conditions (clouds, mist, etc.), the reduction can give a wrong spectral slope and, consequently, the errors in scaling the Hα wavelength band can be large. Most of the spectra from the 1-m and 6-m SAO telescopes were obtained separately in the blue (Hβ) and in the red (Hα) bands, with a resolution of 8−9 Å. Usually, the red edge of the blue spectra and the blue edge of the red spectra overlapped within an interval of ∼300 Å. Therefore, as a zero approximation (the first stage), the majority of red spectra was scaled using the overlapping continuum region with the blue spectra, which were scaled with the [O III]λ 5007 line. In this case the scaling uncertainty is about 5%−10%. However, for some red spectra, this method could not be used because (i) some spectra obtained with a higher resolution (∼5 Å) did not overlap with blue spectra; (ii) some spectrum ends were distorted by the reduction procedures of the instrumental set-up; or (iii) the blue and red spectra were not taken during the same night. Therefore, to increase the precision of the Hα spectral region (the second stage), all red spectra were once more scaled to a constant flux value of the narrow emission line [OI]λ6300, using the modified method of Van Groningen & Wanders (1992; see also Shapovalova et al. 2004). As a reference, we used a red spectrum obtained with the GHAO 2.1-m telescope during a good photometric night, and well-scaled by the [OIII]λ5007 line. After scaling all red spectra using the [OI]λ6300 Å line, we were able to estimate the quality of each spectrum by comparing the [OI] and the [OIII] scalings, and we eliminated the low quality spectra in the further analysis. The uncertainty of the scaling of red spectra by the line [OI]λ6300 (i.e. actually by the flux of the [OIII]λ5007 line) was then about (2−3)%.

Then from the scaled spectra we determined an average flux in the continuum at the observed wavelength ∼5117 Å (i.e. at ∼5100 Å in the rest frame of NGC 4151, $z = 0.0033$), by averaging the fluxes in the band 5092−5142 Å. To determine the observed Hβ and Hα fluxes, it is necessary to subtract the continuum. The continuum was estimated in 30 Å windows, and was fitted by a straight line between two windows centered at 4590 Å and 5125 Å for Hβ, and at 6200 Å and 6830 Å for Hα. After subtracting the continuum, we measured the observed fluxes in the lines, in the following wavelength intervals: 4780−4950 Å for the Hβ and 6415−6716 Å for Hα.

To measure the fluxes of Hγ and HeIIλ4686, we used only 115 blue spectra from a total of 180. The remaining 65 blue spectra were not suitable, because they begin at $\lambda > 4300$ Å, or had a bad correction for spectral sensitivity at the edge of the blue region (for example, because of bad weather). The underlying continuum for Hγ and HeII λ4686 was fitted by a straight line using estimates of the continuum in a 30 Å window centered at 4230 Å and 5125 Å respectively. After continuum subtraction, the Hγ and HeIIλ4686 fluxes were measured in the following wavelength intervals: 4268−4450 Å for Hγ and 4607−4783 Å for HeII λ4686.

[1] See Appendix A in Shapovalova et al. (2004).

2.3. Correction for the position angle (PA), seeing, and aperture effects

To investigate the long-term spectral variability of NGC 4151, it is necessary to have a consistent set of spectra. Since NGC 4151 was observed with different telescopes, in different position angles, and with different apertures, we first had to perform corrections for the position angle (PA), seeing, and aperture effects. A detailed discussion on the necessity for these corrections is given in Peterson et al. (1995), so will not be repeated here.

2.3.1. Correction for the position angle (PA) effect

The position angle corresponds to the position of the slit of the spectrograph on the sky (from North to East). Usually, the observations were performed with PA = 90°, but sometimes it was not possible, e.g. at the 6 m – Nesmith focus, etc. Note that the atmospheric dispersion was very small, since the object was always observed close to the meridian (<2 h and $z < 30°$). To make the correction for the position angle, 80 spectra of NGC 4151 were taken with the 1-m and 6-m SAO telescopes on May 8 and 9, 2003, under photometric conditions and a good seeing (1.2″–1.5″), in different position angles (PA = 0, 45, 90, 135 degrees), and with different spectrograph entrance slits (1″, 1.5″, 2″, 4″, 8″). Data sets with PA = 90 degrees for different slits were used as the standard, since most of the NGC 4151 spectra in our monitoring campaign were obtained in this position angle. Then we determined corrections for the PA effect k(PA), as

$$k(\mathrm{PA}) = F(90)/F(i),$$

where $F(i)$ is the observed flux at PA = i degrees, and $F(90)$ the flux obtained at PA = 90 degrees. In Table 3 (available only in electronic form), we list the PA corrections k(PA) for the Hβ and continuum fluxes, obtained for PA = 0, 45, and 135 degrees, with apertures 2.0″ × 6.0″ and 4″ × 20.25″. As can be seen from Table 3, the variations in k(PA) between the Hβ and continuum fluxes in the same PA is small (<1%), except for PA = 45 degrees where they are <3%. A maximum PA correction for the continuum flux, kp(cnt) = 1.1, was obtained with PA = 45 degrees and an aperture 2″ × 6.0″. This PA nearly corresponds to the axis of the ionized cone (PA ∼ 50 degrees). The line and continuum fluxes were determined for PA = 90 degrees, using a linear interpolation of the k(PA) values of Table 3.

2.3.2. Correction for the seeing effect

The narrow line region (NLR) of NGC 4151 has an extended biconical structure spreading up to >2″ from the nucleus (Evans et al. 1993), while the BLR and non-stellar (AGN) continuum are effectively point-like sources (≪1″). Consequently, the measured NLR flux depends on the size of the spectrograph entrance aperture (see Peterson et al. 1995, for a detailed discussion). Also, since we observed with different telescopes and apertures, for each aperture the measured ratio of the BLR flux (a point-like source) to the NLR flux (a spatially extended region) depends on the seeing. Therefore, in each aperture we must find corrections for images and reduce all flux data to some accepted standard image. The method suggested by Peterson et al. (1995) has been used for this purpose. For the seeing in each aperture we can write

$$F(s) = k(s) \cdot F(\mathrm{PA}) - G(s)$$

where F(PA) is the observed flux at PA = 90 degrees, $F(s)$ the seeing corrected flux, $k(s)$ a point-source correction factor, and $G(s)$ an extended source correction taking the host galaxy light into account. Obviously, $G(s) = 0$ for the broad-line flux (point-like source).

We divided the whole range of seeing values into several intervals, for two different apertures. For the first aperture, 2.0″(2.5″)×6.0″, which corresponds to the observations with the 6-m and 2.1-m telescopes (México), we considered the following intervals: 1″–1.5″, 1.5″–2.5″, 2.5″–3.5″, 3.5″–4.5″, and >4.5″. The data set for the interval 1.5″–2.5″ was adopted as a standard one since the average seeing in the period of observations with this aperture was about 2″. A value $k(s) = 1$ and $G(s) = 0$ was accepted for this standard data set. We obtained the seeing correction $k(s)$ and the extended source correction $G(s)$ for the seeing intervals mentioned above using spectra observed with different seeings within a time interval shorter than 3 days, i.e., $k(s) = F(1.5''–2.5'')/F(\mathrm{PA})_i$, where $F(\mathrm{PA})_i$ is the observed flux in PA = 90 for the i-seeing, and $F(1.5''–2.5'')$ is the flux for the seeing interval 1.5″–2.5″; these data are separated by 3 days or less. In Table 4 (available only in electronic form), we listed the $k(s)$ and $G(s)$ corrections and the data obtained from Peterson et al. (1995, their Figs. 5 and 6) for the aperture 2″ × 10″ From this table, one can see that our seeing corrections $k(s)$ for an aperture of 2″ × 6″ practically coincide (within 1%) with those of Peterson et al. (1995) for an aperture of 2″ × 10″. The correction ($k(s)$ in Table 4) for the emission line fluxes is the same for a slit length of 6″ and of 10″, meaning that the lines are emitted by a region smaller than 6″, but there are significant differences in the host galaxy contribution, as expected.

For the second aperture, 4.2″ × 19.8″, which corresponds to our observations with the 1-m Zeiss telescope (SAO), we used the seeing intervals 2″–4″, 4″–6″, 6″–8″. They are large because with this telescope it is impossible to determine the seeing quality with a good precision, owing to the small scale along the spectrograph slit (2.2″/px). The data set for the interval 2″–4″ was used as a standard. The seeing corrections $k(s)$ and $G(s)$ for the aperture 4.2″ × 19.8″ were obtained with the same procedure described above for the aperture 2″ × 6″. The results are given in Table 5 (available only in electronic form), together with those of Peterson et al. (1995) for the aperture 5″ × 7.5″ (their Figs. 5 and 6).

Emission line and continuum fluxes were scaled to the mean seeing 2″ for the apertures 2″ × 6.0″(2.5″ × 6.0″) and to the mean seeing 3″ for the aperture 4.2″ × 19.8″, using the seeing corrections from Tables 4 and 5. After that, we scaled all spectra to the 2″ × 6.0″ aperture (cf. below).

2.3.3. Correction for the aperture effect

To correct the observed fluxes for aperture effects, we determined a point-source correction factor φ using the equation (see Peterson et al. 1995, for a detailed discussion):

$$F(\mathrm{Hb})\mathrm{true} = \varphi \cdot F(\mathrm{Hb})\mathrm{obs},$$

where F(Hb)obs is the observed Hβ flux after correction for the PA and seeing effects, as described in Sects. 2.3.1 and 2.3.2; F(Hb)true is the Hβ flux corrected for the aperture effect.

The contribution of the host galaxy to the continuum flux also depends on the aperture size. The continuum fluxes $F_\lambda(5117)$ were corrected for different amounts of host-galaxy contamination, according to the following expression (see Peterson et al. 1995):

$$F(5117\ \text{Å})\mathrm{true} = \varphi \cdot F(5117\ \text{Å})\mathrm{obs} - G(g),$$

Table 6. Flux scale factors for optical spectra.

Sample	Years	Aperture (arcsec)	Point-source Scale factor (φ)	Extended source Correction G(g)[a]
L(U,N)	1996–2005	2.0×6.0	1.000	0.000
GH,S-P	1996–2005	2.5×6.0	1.000	0.000
L(S)	2004–2006	1.0×6.0	0.950 ± 0.000	–0.391
L1(G)	1996–2003	4.2×19.8	1.035 ± 0.021	1.133 ± 0.037
L1(G)	1996–2003	8.0×19.8	1.112 ± 0.005	1.623 ± 0.080
L1(U)	2004–2006	4.0×9.45	0.962 ± 0.044	0.750 ± 0.150

[a] In units 10^{-14} (erg s^{-1} cm^{-2} Å^{-1}).

where $F(5117A)$obs is the observed continuum flux after correction for the PA and seeing effects, as described in Sects. 2.3.1 and 2.3.2; $G(g)$ is an aperture – dependent correction factor to account for the host galaxy contribution. The cases L (Table 1), which correspond to the aperture ($2'' \times 6''$) of the 6-m telescope, was taken as a standard (i.e. $\varphi = 1.0, G(g) = 0$ by definition). The corrections φ and $G(g)$ were defined for each aperture via the comparison of a pair of observations separated by 0 to 2 days. It means that the variability on shorter times (<2 days) was suppressed by the procedure of data re-calibration. The point-source correction factors φ and $G(g)$ values for various samples are given in Table 6. Using these factors, we re-calibrated the observed fluxes of Hα, Hβ, Hγ, and HeIIλ4686 and of the continuum to a common scale corresponding to the aperture $2'' \times 6''$ (Table 7 – available only in electronic form).

The fluxes listed in Table 7 were not corrected for contamination by the narrow-line emission components of Hγ, HeIIλ4686, Hβ, Hα, and [N II]$\lambda\lambda$ 6548, 6584. These contributions are expected to be constant and to have no influence on the broad line variability.

The mean error (uncertainty) in our flux determinations for Hα and Hβ and for the continuum is <3%, while it is ~5% for Hγ and ~8% for HeII λ4686. These quantities were estimated by comparing the results from spectra obtained within time intervals shorter than 2 days. The estimated mean errors for every year and for the total period of monitoring are given in Table 8 (available only in electronic form).

2.4. The narrow emission line contribution

To estimate the narrow line contributions to the broad line fluxes, we constructed a spectral template for the narrow lines. To this end, we used the blue and red spectra in the minimum activity state (May 12, 2005), obtained with a spectral resolution of ~8 Å. In these spectra, the broad Hβ component was very weak, and the broad components from the higher Balmer line series were absent.

Both the broad and the narrow components of Hγ, HeIIλ4686, Hβ, and Hα were fitted by Gaussians. The template spectrum contains the following lines: for Hγ: the narrow component of Hγ and [O III]λ4363; for Hβ: the narrow component of Hβ and [O III]$\lambda\lambda$4959, 5007; for Hα: the narrow component of Hα, [N II]$\lambda\lambda$ 6548, 6584, [O I]$\lambda\lambda$ 6300, 6364) [S II]$\lambda\lambda$ 6717, 6731 and HeI λ 6678. Table 9 lists the narrow line contributions obtained from the template spectrum in the same wavelength integration intervals as for integral fluxes. Our results are in good agreement with those given by Sergeev et al. (2001).

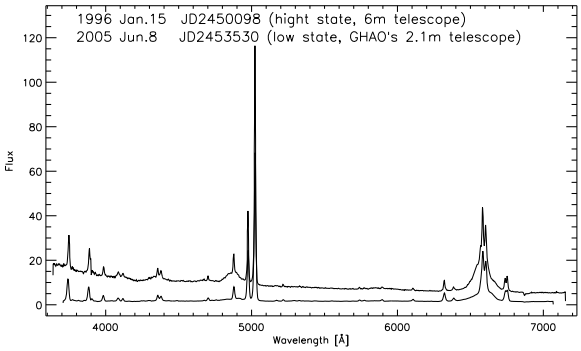

Fig. 1. The spectra of NGC 4151 corresponding to the high activity state (*top*) and to the low activity state (*bottom*). The observed wavelength (we recall that $z = 0.0033$) is displayed on the X-axis, and the flux (in units of 10^{-14} erg cm^{-2} s^{-1} Å^{-1}) is displayed on the Y-axis.

3. Data analysis

3.1. Variability of the emission lines and of the optical continuum

The spectra for the high- and low-activity states, obtained respectively on January 15, 1996 (6 m SAO's telescope) and on June 8, 2005 (2.1 m GHAO's telescope) are presented in Fig. 1. As can be seen, the continuum flux decreased by a large factor (~5.6 times) in the low-activity state, and the slope of the continuum in the blue was significantly flatter than in the high-activity state. Besides, the wings of Hβ and Hα became extremely weak in the minimum state, and those of Hγ and of the higher Balmer line series could not be detected at all. These profiles correspond to a Sy 1.8 type and not to a Sy1-Sy1.5, as this AGN could be classified in the maximum state; hence, the spectral type of the object is changing with time. This was noted earlier. In 1984–1989, the nucleus of NGC 4151 went through a very deep minimum. At that time, the brightness of the source fell down to the level of the host galaxy for an aperture of 27″ in the V-band, the broad wings of hydrogen lines became much weaker (they almost completely vanished in April 1984) and the spectrum of the nucleus was identified as a Sy 2 (Penston & Perez 1984).

In Fig. 2 the light curves obtained from Table 7 are presented for the Hα, Hβ, Hγ, and HeIIλ4686 integrated line fluxes and for the continuum at the observed wavelength 5117 Å. The fluxes of Hγ, HeIIλ4686, Hβ, and Hα were not corrected for contamination by the constant contributions of the narrow lines. The contributions of the narrow lines given in Table 9 are also shown. It is clearly seen that, if the fluxes of the narrow lines are subtracted from Hγ and HeIIλ4686 during the minimum of activity, these lines disappear.

The continuum flux presented in Table 7 and in Fig. 2 also contains a constant contribution from the starlight of the host galaxy, which is estimated as $F(\text{host}) = 1.54 \times 10^{-14}$ erg cm^{-2} s^{-1} Å^{-1} through an aperture of 5″×7.5″ (Peterson & Cota 1988), and 10^{-14} erg cm^{-2} s^{-1} Å^{-1} through an aperture of $3'' \times 10''$ (Mal'kov et al. 1997). Bochkarev et al. (1991) determined that the host galaxy contributed to about 40% of the total flux of NGC 4151 in the Hβ wavelength band though an aperture $1'' \times 4.0''$, near the minimum state (1987). As can be seen from Table 7, the minimum flux in the continuum (~1.6×10^{-14} erg cm^{-2} s^{-1} Å^{-1}) obtained with an aperture $2'' \times 6''$ was observed from November 29 to December 17, 2000. If we assume that the host galaxy contribution is about 40%

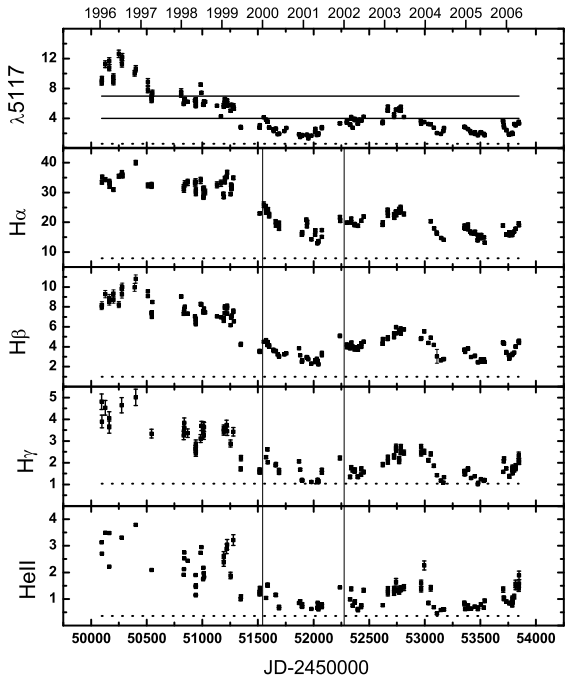

Fig. 2. The light curves of Hα, Hβ, Hγ, HeIIλ4686 and of the continuum at the observed wavelength λ = 5117 Å, in the period 1996–2006. Constant contributions from the narrow lines (Table 9) and from of the host galaxy (see Sect. 3.1) are shown by horizontal dashed lines. The line fluxes are given in units of 10^{-12} erg cm^{-2} s^{-1}, and the continuum flux in units of 10^{-14} erg cm^{-2} s^{-1} Å^{-1}. The horizontal lines in the first panel correspond to the division of the continuum flux into three intervals (see Sect. 3.4.2), and the vertical lines correspond to the division into time intervals based on the similarity of the line shapes (see Sect. 3.3).

Table 9. The wavelength integration intervals and the corresponding NLR contributions.

Components	Integration intervals (Å)	NLR flux[a]
Hα+[NII]	6415–6716	7.93
Hβ-nar.	4780–4950	1.00
Hγ+[OIII]λ4363	4268–4450	1.04
HeII+[ArIV]+ [FeIII] 4658	4607–4783	0.36

[a] In 10^{-12} erg cm^{-2} s^{-1}.

of the continuum (Bochkarev et al. 1991), it gives F(host) > 0.6×10^{-14} erg cm^{-2} s^{-1} Å^{-1} (i.e. lower limit). Using a linear regression between the continuum flux and the Hα and Hβ broad line fluxes (the narrow line flux being subtracted) near the low-activity state, and extrapolating the broad line flux to zero, we estimated F(host) $\approx (0.6\pm0.3)\times10^{-14}$ erg cm^{-2} s^{-1} Å^{-1}. This value is in good agreement with other estimates with different apertures. The estimated contribution from the host galaxy is also given in Fig. 2 (top). The light curve of the continuum is similar to those of the emission lines, showing a maximum in 1996 and two minima in 2001 and 2005.

In Table 10, we give for the lines and continuum, the mean observed maximum flux $F_{\rm obs}^{\rm max}$ in the interval JD = 2 450 094–2 450 402 (1996), the mean observed minimum flux $F_{\rm obs}^{\rm min}$ in the intervals JD = 2 451 895–2 452 043 (December 2000–May 2001), and JD = 2 453 416–2 453 538 (2005), the observed ratio $R_F = F_{\rm obs}^{\rm max}/F_{\rm obs}^{\rm min}$ and this ratio for the

Table 10. Line and continuum fluxes. See the text for the definition of the parameters.

Lines or continuum[a]	$F_{\rm obs}^{\rm max}$	$F_{\rm obs}^{\rm min}$	R_F	$R_F^{\rm broad}$
Hα	34.860	15.340	2.3	3.6
Hβ	9.170	2.640	3.5	5.0
Hγ	4.365	1.178	3.7	24!(not broad)
HeIIλ4686	3.170	0.714	4.4	7.9
cont(5117A)	10.69	1.9	5.6	7.8 agn continuum

[a] Line fluxes are in units 10^{-12} erg cm^{-2} s^{-1}; and continuum flux is in units 10^{-14} erg cm^{-2} s^{-1} Å^{-1}.

Table 11. The wavelength intervals for the Hα and Hβ wings and cores.

Component	Integration interval in Å	Integration interval in km s^{-1}
Hα blue wing	6486–6552	(–4510)–(–1503)
Hα core	6553–6616	(–1458)–(+1402)
Hα red wing	6617–6684	(+1458)–(+4510)
Hβ blue wing	4804–4853	(–4493)–(–1479)
Hβ core	4854–4900	(–1417)–(+1412)
Hβ red wing	4901–4950	(+1474)–(+4488)

broad lines $R_F^{\rm broad}$ after subtraction of the narrow components and the contribution of the host galaxy (agn continuum in Table 10).

The maximum amplitude ratios of the broad component line flux during the 1996–2006 period were ~3.6 for Hα, ~5.0 for Hβ line, and ~7.8 for the λ5117 Å agn continuum after subtraction of the host galaxy flux. In the low-activity state, the broad component of HeIIλ4686 and Hγ was almost absent.

3.2. Flux variability in the wings and core of the Hα and Hβ emission lines

We divided the Hα and Hβ profiles into three parts: the blue wing, the core, and the red wing, each part covering a range of 3000 km s^{-1}. Distinct features or peaks observed at different epochs in the wings were included, and the corresponding narrow lines were included in the core. In Table 11, we give the wavelength intervals used to measure the flux in the three parts of each profile. We also give the corresponding velocity intervals with respect to the center of the narrow component.

Light curves for the wings and cores of Hα and Hβ are presented in Fig. 3. As can be seen, the flux in the wings and cores of both lines behaved similarly during the monitoring period.

In Fig. 4 we present the flux ratios between the three parts of the Hα and Hβ profiles. In both lines, the blue wing had a stronger flux than the red one in the period of maximal activity (March 1996 to 1997 or JD = 2 450 094–2 450 500) (F(blue)/F(red) > 1, see Fig. 4, top-left). From 1997 to 2000 (or JD = 2 450 540–2 451 500), the Hα blue/red flux ratio was very close to unity, while the Hβ blue/red ratio varied from 0.95 to 0.8 (Fig. 4, top-right). In 2000–2006 (JD = 2 451 550–2 453 850), the red wing was the strongest for both lines, and the Hα blue/red ratio decreased almost monotonically from 0.8 to 0.6 (Fig. 4, top-left), while it varied from 0.6 to 0.8 for Hβ (Fig. 4, top-right).

The F(blue)/F(core) ratio of both lines was decreasing nearly monotonically from 1996 to 2001 (JD = 2 450 094–2 452 000). After 2002 (JD > 2 452 300), the

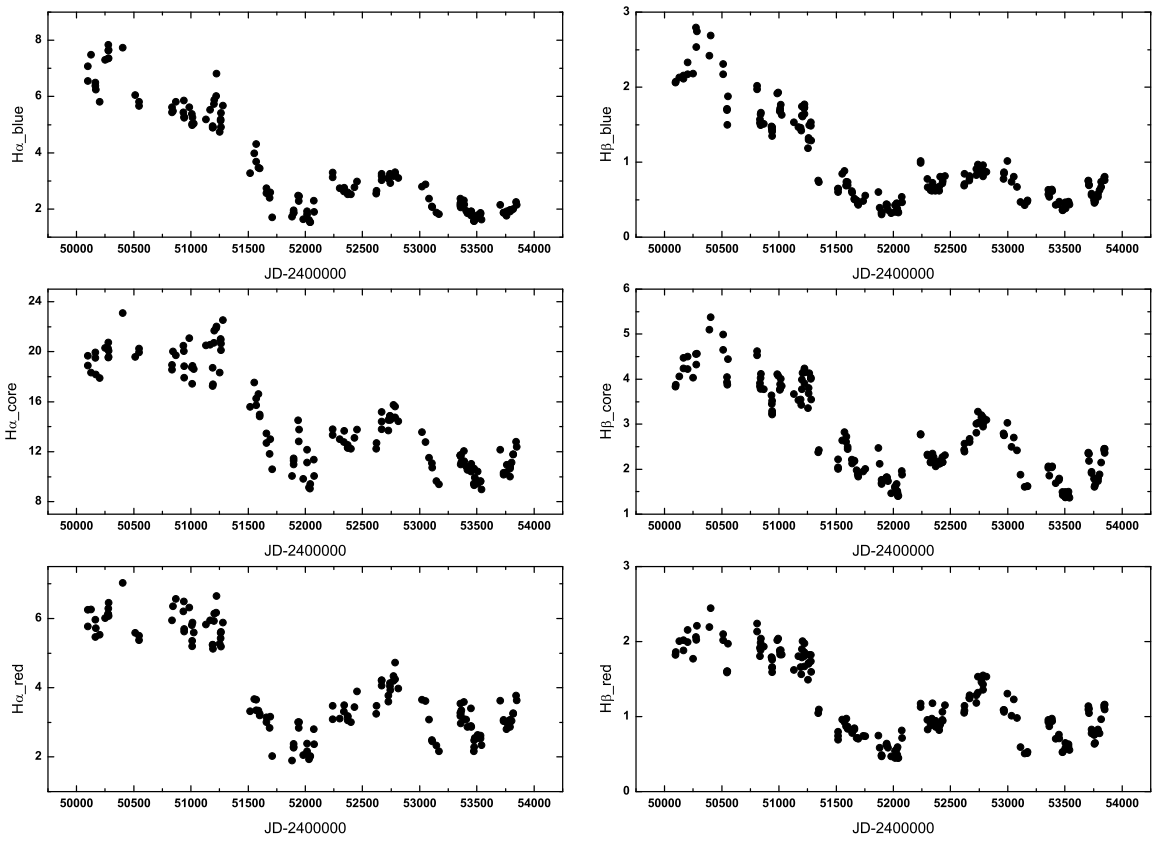

Fig. 3. The variation of the wings and core of Hα (*left*) and Hβ (*right*) from 1996 to 2006. The flux is given in units of 10^{-12} erg cm^{-2} s^{-1}.

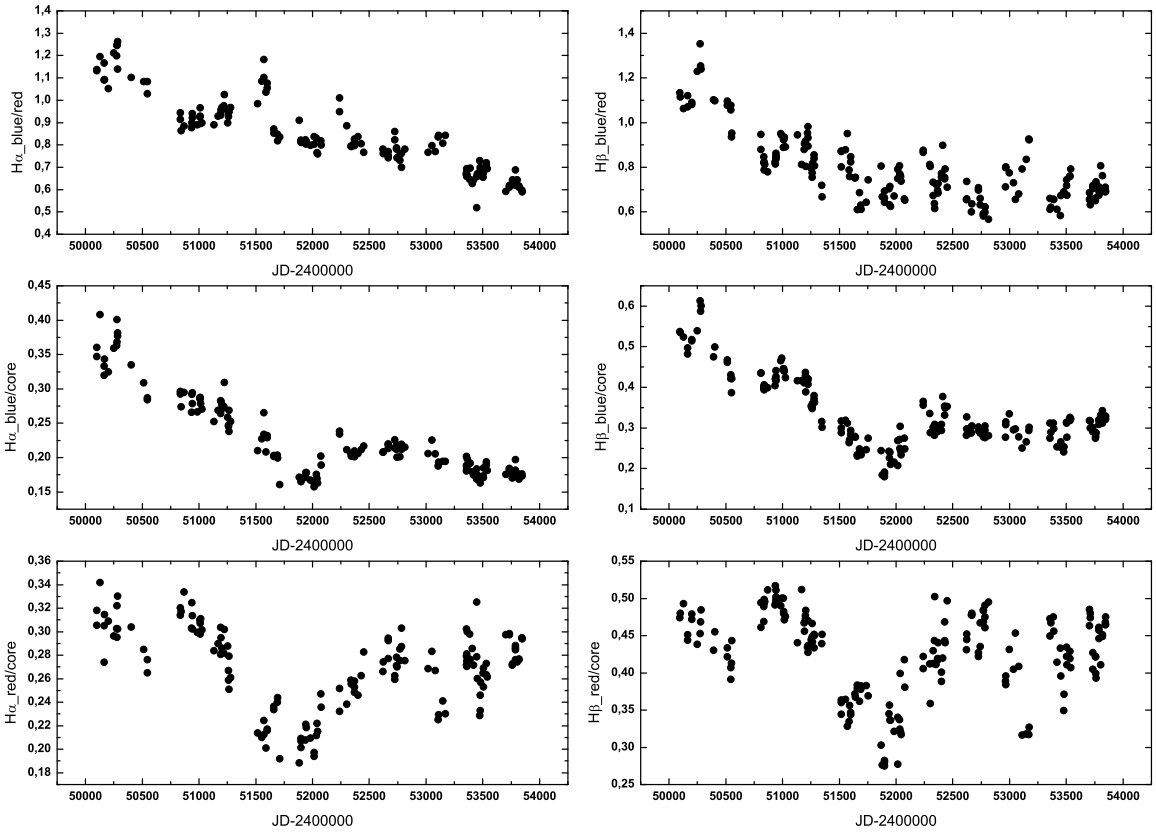

Fig. 4. The variation in the ratio of the fluxes in the line wings and in the core of Hα (*left*) and Hβ (*right*) (see the text), from 1996 to 2006.

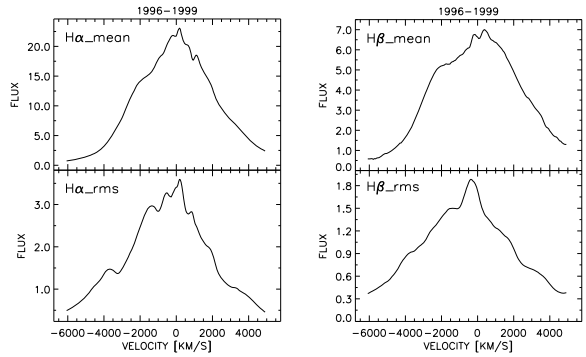

Fig. 5. The averaged and rms profiles of the broad Hα (*left*) and Hβ (*right*) lines for the first period.

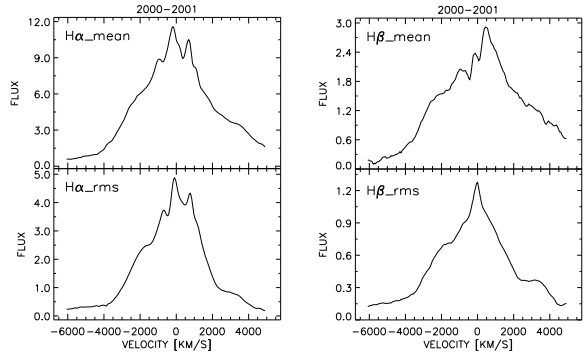

Fig. 6. The averaged and rms profiles of the broad Hα (*left*) and Hβ (*right*) lines for the second period.

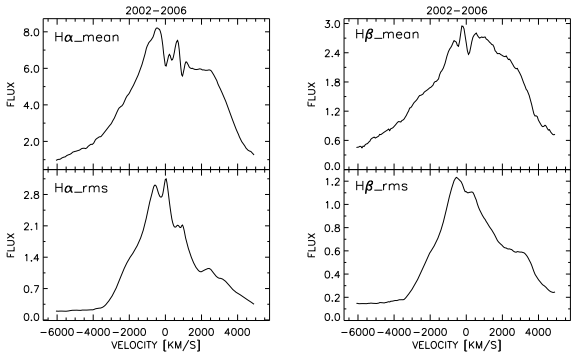

Fig. 7. The averaged and rms profiles of the broad Hα (*left*) and Hβ (*right*) lines for the third period.

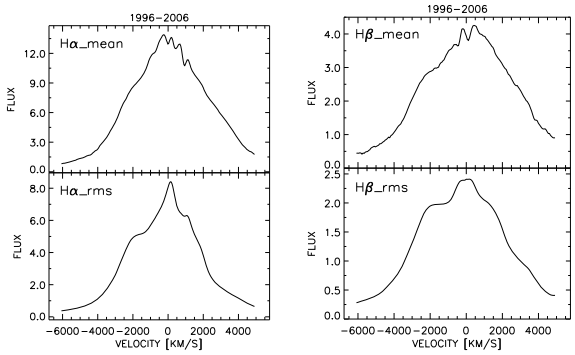

Fig. 8. The averaged and rms profiles of the broad Hα (*left*) and Hβ (*right*) lines for the whole monitoring period.

Hβ ratio remained nearly constant (≈0.3), while the Hα ratio decreased very slightly (Fig. 4, middle). On the other hand, the F(red)/F(core) ratio of both lines showed approximaly the same rapid changes in the monitoring period.

3.3. Mean and root-mean-square spectra

The comparison between the averaged and the root-mean-square (rms) spectra allows the line profile variability be investigated. We first inspected the Hα and Hβ profiles for different periods, using spectra with a resolution of 8 Å. With a criteria based on the similarity of line profiles, we found three characteristic profiles during the period 1996−2006. In the first period (1996−1999, JD = (2 450 094.466−2 451 515.583), where the lines were very intense, a red asymmetry and a shoulder in the blue wing were present. In the second period (2000−2001, JD = 2 451 552.607 − 2 452 238.000), the broad lines were weaker and the shoulder in the blue wing is smaller and a shoulder in the red part is present. From 2002 to 2006 (third period, JD = 2 452 299.374−2 453 846.403), the lines showed a blue asymmetry, and a shoulder in the red part was dominant in the line profiles (peak at $\lambda \approx 4915$ Å or at ≈2000 km s^{-1} relative to the narrow component, see Figs. 5−7, top).

Averaged and rms profiles of Hβ and Hα for each of these three periods and for the whole monitoring period (1996−2006) were calculated after removing the continuum. They are shown in Figs. 5−8.

We measured the Full Width at Half Maximum (*FWHM*) in the rms and averaged broad line profiles, and we defined the asymmetry A as the ratio of the red/blue Half Width at Half Maximum (*HWHM*), i.e. $A = HWHM_{\rm red}/HWHM_{\rm blue}$. The measured values for the broad Hβ and Hα lines and their rms are given in Table 12.

As can be seen in Fig. 5 (bottom), the blue component was highly variable in the first period, the rms profile of Hα and in a lesser extent of Hβ, showing two peaks or shoulders at ∼−4000 km s^{-1} and ∼−2000 km s^{-1}. In the red part of the rms profile of Hα, a weak bump at +2000 km s^{-1} and a shoulder at +3500 km s^{-1} was also detected, while only weak shoulders were seen at the same places in the rms profile of Hβ. On the other hand, the line and their rms profiles show a blue asymmetry ($A < 1$, see Table 12). In the second period (see Fig. 6, bottom), the feature at ∼−4000 km s^{-1} in the blue part of the rms profile of both lines disappeared, and only a shoulder at ∼−2000 km s^{-1} was present. The averaged Hα profile has a blue asymmetry, but the Hβ one is almost symmetric. In the red part of the rms profile of both lines, the shoulder seen in the first period at ∼3500 km s^{-1} was still present. This feature, but shifted at 2500 km s^{-1}, was dominant in the third period (Fig. 7), not only in the rms profiles of Hα and Hβ, but also in their averaged profiles. Both lines show a red asymmetry in this period, but it is interesting to note that the Hα rms profile shows a significant blue asymmetry ($A \approx 0.82$), while the Hβ rms profile has a significant red asymmetry ($A \approx 1.17$). Averaged and rms profiles are given in Fig. 8 for the whole monitoring period from 1996 to 2006. As can be seen, two shoulders dominate the rms profiles: a blue one at ∼−2000 km s^{-1} and a red one at ∼1500 km s^{-1}. Also, the variation in the blue part is more significant than in the red one, because the line intensities during the whole monitoring period are dominated by the first period, when the variation in the blue part was the most significant and at the same time the lines were the most intense. Table 12 shows also that for the whole monitoring period, the rms profiles of both lines have

Table 12. The *FWHM* and the ratio $A = HWHM_{\rm red}/HWHM_{\rm blue}$ of the red/blue, for the averaged and rms profiles of Hα and Hβ, during the three periods.

Period	*FWHM* (Hα)	A_α	*FWHM* (Hβ)	A_β
first	4780 ± 350	0.944 ± 0.012	5980 ± 550	0.935 ± 0.048
second	4020 ± 570	0.872 ± 0.053	5550 ± 750	1.086 ± 0.067
third	5790 ± 410	1.491 ± 0.075	6350 ± 430	1.282 ± 0.112
mean profile	4650 ± 420	1.000 ± 0.023	6110 ± 440	1.056 ± 0.018
Period	*FWHM* (rms Hα)	A_α – rms	*FWHM* (rms Hβ)	A_β – rms
first	4790 ± 350	0.810 ± 0.046	5430 ± 530	0.596 ± 0.017
second	3100 ± 480	1.061 ± 0.026	3700 ± 550	0.811 ± 0.068
third	3150 ± 350	0.816 ± 0.038	3760 ± 1100	1.168 ± 0.210
mean rms	4420 ± 320	0.830 ± 0.011	5490 ± 420	0.775 ± 0.023

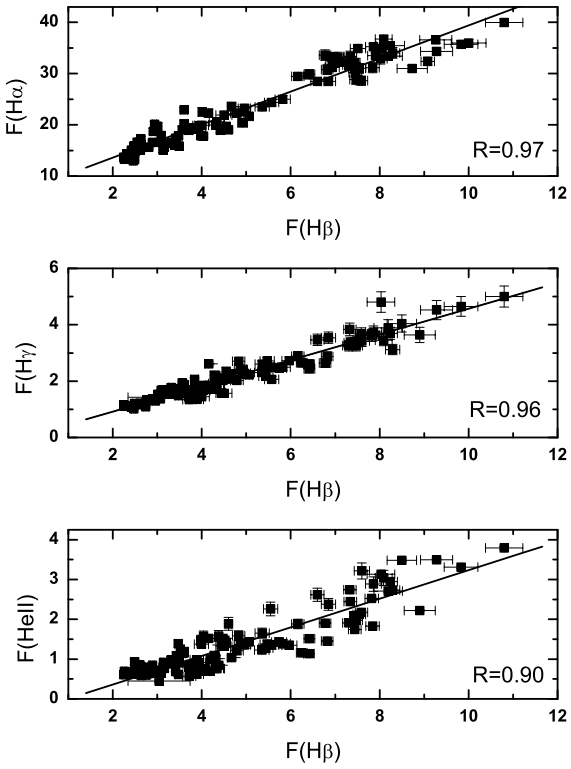

Fig. 9. The Hα, Hγ, HeIIλ4686 fluxes versus the Hβ flux.The correlation coefficients r are given inside the plot. The flux is given in units of 10^{-12} erg cm^{-2} s^{-1}.

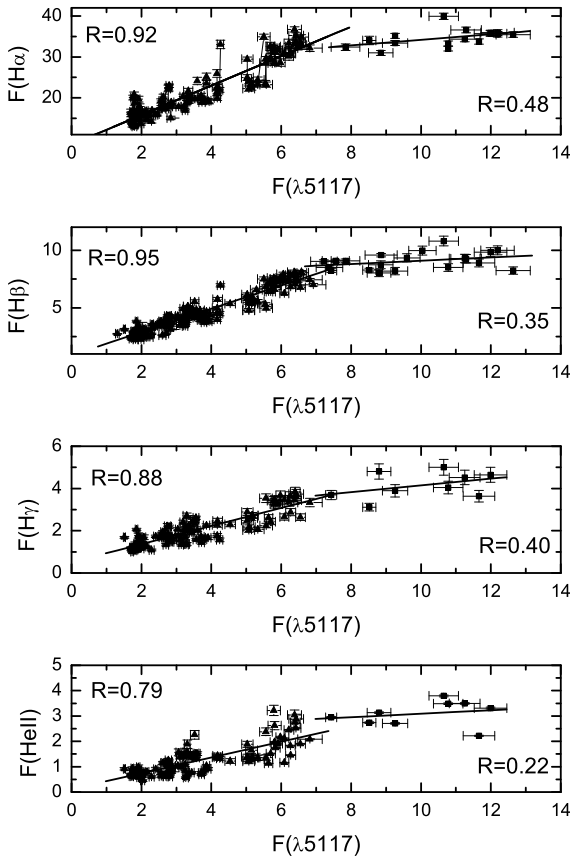

Fig. 10. The Hα, Hβ, Hγ, HeIIλ4686 fluxes versus the continuum flux (at λ = 5117 Å). The correlation coefficients r are given inside the plot. The line fluxes are given in units of 10^{-12} erg cm^{-2} s^{-1}, and the continuum flux in units of 10^{-14} erg cm^{-2} s^{-1}Å^{-1}.

a significant blue asymmetry, and that the averaged and rms *FWHM* of Hβ are larger than those of Hα by about 1000 km s^{-1}.

Such behavior of the rms profiles during the three periods indicate that the BLR of NGC 4151 has a complex structure and that its geometry may change in time. More information about line profiles will be given in a forthcoming paper.

3.4. The line and continuum flux correlations

3.4.1. The line-line and continuum-line relationship

To find the line-line flux relationships we have plotted the fluxes of Hα, Hγ, and Heλ4686 vs. the Hβ flux (Fig. 9). As expected, there is a linear relation between the Hβ flux and that of the other lines. The correlation coefficients between the Hβ flux and the Hα, Hγ, and Heλ4686 fluxes are $r \approx 0.97$, 0.96, and 0.90, respectively. The slight differences between the correlation coefficients may be caused by uncertainty in the measurements (i.e. very weak Hγ and Heλ4686 in some periods)

We have also plotted the Hα, Hβ, Hγ and Heλ4686 fluxes against the continuum flux Fc (see Fig. 10). We find that the relationship between the line and continuum fluxes can be divided into two separated sequences. The first sequence, corresponding to $Fc \lesssim 7\times10^{-14}$ erg cm^{-2} s^{-1} Å^{-1}, took place in the period 1998 to 2006; there was a linear relationship between the lines and continuum fluxes with a high correlation coefficient (0.88–0.95) for the Balmer lines. The behavior of Heλ4686 vs. Fc is not clear, tending to be linear, but with a high dispersion (r = 0.79) when Fc was equal to $5.5–7 \times 10^{-14}$ erg cm^{-2} s^{-1} Å^{-1}, corresponding to the period 1998–1999. The second sequence

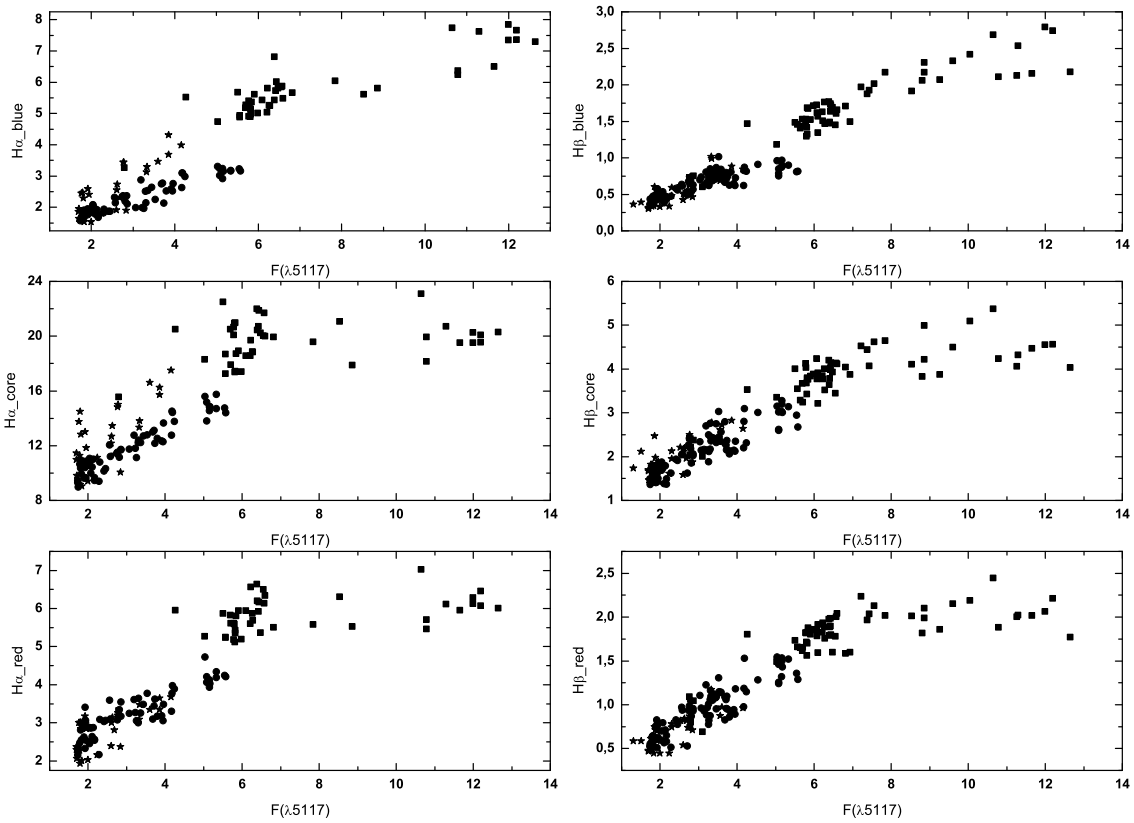

Fig. 11. The wings and core fluxes as a function of the continuum flux (at λ = 5117 Å) for Hα (*left*) and Hβ (*right*). The line and continuum fluxes are given in the same units as in Fig. 10.

corresponds to high values of Fc ($\gtrsim 7 \times 10^{-14}$ erg cm^{-2} s^{-1} Å^{-1}) and belongs to the period from 1996 to 1997. Here the line fluxes tended to remain constant, with a very weak correlation with Fc (see Fig. 10; $r \sim 0.2$–0.48 is given in the right-down corner for each line).

In Fig. 11 we show the relation between the continuum flux and the different parts of the Hα and Hβ profiles (the blue, the core, and the red). As can be seen, the relation for the core and the blue/red wing is similar to that of the whole line (see Fig. 10).

To find an explanation for this behavior, we inspected these relationships within the three periods of observations mentioned above (see Sect. 3.3). We concluded that there was not only a difference in the line profiles, but also in the continuum vs. line flux relationships.

In the first period, when the lines were the most intense, there was a weak correlation between the lines and the continuum fluxes. The Hα flux changed by only $\sim\pm$40%, while the continuum flux changed by a factor three (see Fig. 12, left). During the same period, Hβ was also very weakly correlated to the continuum (Fig. 12, right), except for five points, corresponding to observations between June and December 1999. At this time the continuum and Hβ fluxes nearly decreased by a factor two, but the Hβ and Hα profiles remained almost identical. In the second period, a large dispersion was observed for $Fc \lesssim 3.3 \times 10^{-14}$ erg cm^{-2} s^{-1} Å^{-1}, and the lines did not respond to the continuum. Some points (5) with $Fc \geq 3.3 \times 10^{-14}$ erg cm^{-2} s^{-1} Å^{-1} in Fig. 12 (middle) correspond to spectra taken in January and February 2000, and their Hα and Hβ profiles are similar to those in the first period (i.e. they have a red asymmetry and a shoulder in the blue wing). In the third period, the response of the lines to the continuum was linear.

3.4.2. Cross-correlation analysis

To determine the time lag between the optical continuum and the line variations (line lagging continuum), we used the cross correlation function – CCF method introduced by Alexander (1997), the z-transformed discrete correlation function (ZDCF), which contains the idea of the discrete correlation function (DCF) method (Edelson & Krolik 1988) avoiding an interpolation. The ZDCF approximates the bin distribution by a bi-normal distribution. This algorithm differs from the DCF in that the data points are equally binned, and it uses Fisher's z-transform to stabilize a highly-skewed distribution of the correlation coefficient. According to Alexander (1997), ZDCF is much more efficient than DCF in detecting correlations involving the variability time scale, and it is more sensitive to under-sampled light curves than DCF and interpolated cross-correlation function (Gaskell & Sparke 1986; Gaskell & Peterson 1987).

The CCF analysis was carried out for the full data set which covers the whole monitoring period from 1996 to 2006 and the three periods mentioned above. The time lags and CCF for Hβ and Hα are given in Table 13. The CCF coefficients are calculated between the continuum flux and the Hα, Hβ fluxes (line lagging contninuum). Positive time lags mean that the line light curve lags behind the continuum light curve.

We also calculated the CCF and the time lags by dividing the data set into three groups according to the continuum intensity: (i) $F^1_{\rm con} \geq 7 \times 10^{-14}$ erg cm^{-2} s^{-1} Å^{-1}; (ii) $7 \times 10^{-14} > F^2_{\rm con} \geq 4 \times 10^{-14}$ erg cm^{-2} s^{-1} Å^{-1} and (iii) $F^3_{\rm con} < 4 \times 10^{-14}$ erg cm^{-2} s^{-1} Å^{-1}. As seen in Fig. 12, $F^1_{\rm con}$ is only present during the first period, while $F^2_{\rm con}$ and $F^3_{\rm con}$ are present in all three periods. Table 13 shows that, for such a division, the CCF is small when the continuum is high. There is a big difference in the

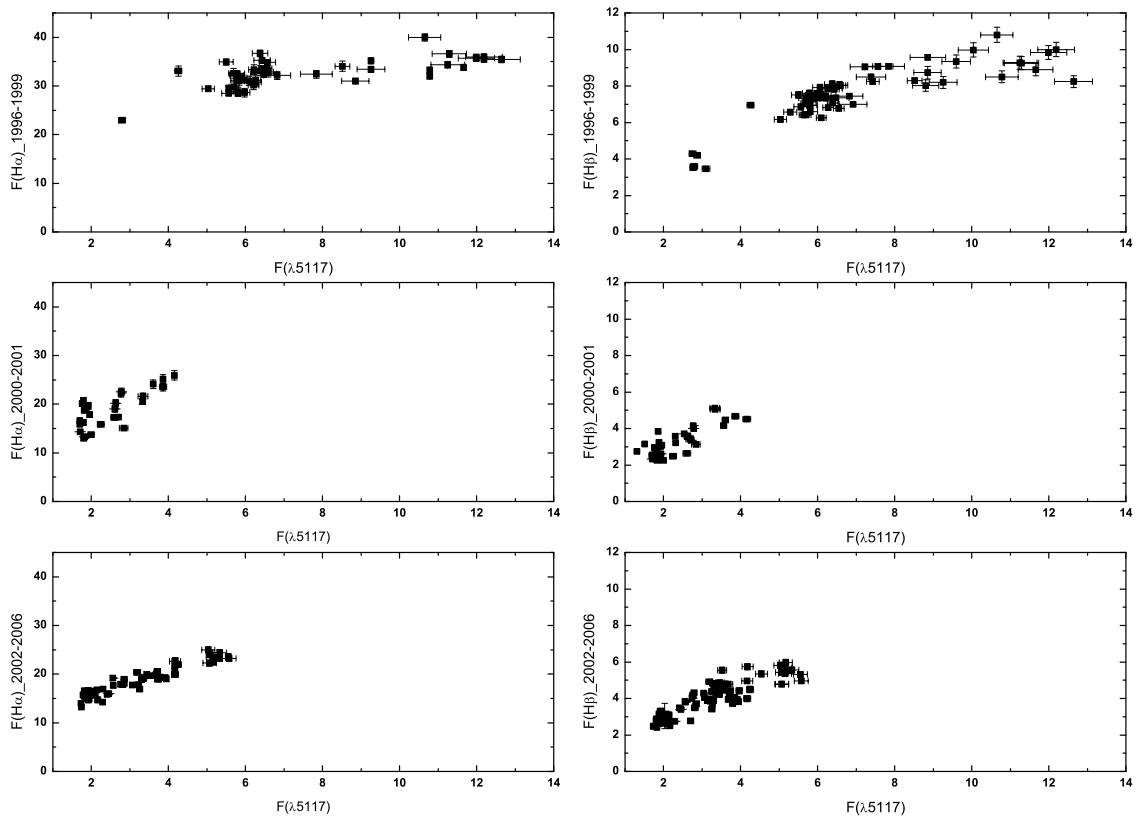

Fig. 12. Hα (*left*) and Hβ (*right*) fluxes for the three periods (first to third *from top to down*) as a function of the continuum flux. The line and conntinuum fluxes are given in the same units as in Fig. 10.

time lags between these three cases. Note that the highest CCF is obtained for the lowest continuum, but it is still smaller than the one obtained in the third period based on the line profiles. The time lags for Hα and Hβ in the whole period are ~5 days, but they were different in the three periods. In the first and third periods, the time lags were much shorter for both lines (from 0.6 to 1.1 days) than in the second period (11 and 21 days).

The time lags should, however, be considered as having a relative significance, since the CCF curves are very messy, as seen from the large uncertainties of the results, and some curves are asymmetrical. To illustrate this, we give the shifts of the centroïds in light-days in Table 13, when they could be measured. All these results together indicate a complex line-to-continuum response, due to complex and varying BLR.

We can summarize the CCF analysis as follows.

1. The correlation between continuum and line flux is strongest at lowest continuum flux levels, and so the CCF is best defined during these periods, i.e. in periods 2 and 3. During these periods, the peak of the CCF was closer to zero than is the centroid of the CCF;
2. at high flux periods, the CCFs are defined less well, so it is very difficult to define any lag;
3. the CCF is generally asymmetric, implying line emitting gas at a range of radii, from close in (1 light-day) to far out (50 light-days).

4. Discussion

During the monitoring period, the spectrum of NGC 4151 underwent strong changes, not only in the line and continuum fluxes, but also in the Hβ and Hα line profiles. Using the line profiles, we characterized three periods (see Sect. 3.3, Tables 12 and 13, and Fig. 12). We found that the *FWHM* of Hα and Hβ are different, Hβ being significantly broader than Hα (~1000 km s^{-1}). This may indicate that Hβ is formed deeper in the BLR, i.e. closer to the black hole. On the other hand, the blue asymmetry in the averaged rms of Hβ and Hα could indicate a contribution of the emitting gas with an approaching motion, i.e. an outflow. Finally, the presence of the central spike in the rms spectrum is hard to explain unless it is produced by a remote component with an axisymmetric distribution and no outward motion. One suggestion is that it comes from a region heated and ionized by the jet. In conclusion, there seems to be at least two BLR components, the first closer and in outward motion, the second located further away with no outward motions. We leave for the following paper a detailed discussion based on the study of the line profiles, and we focus here on the global line variations.

We found that the responses of the Hβ and Hα fluxes to the continuum flux were different in the three periods, but it could be due to the limited range of fluxes in periods 2 and 3. For low values of the continuum flux ($Fc \leq 6 \times 10^{-14}$ erg cm^{-2} s^{-1} Å^{-1}), there was a linear relation between the lines and the continuum in the second and third periods (see Fig. 12). The dispersion of the points is larger in the second than in the third period, so we think that the results concerning the last period are more reliable. Note that Fc is smaller than 4×10^{-14} erg cm^{-2} s^{-1} Å^{-1} in period 2 and smaller than 6×10^{-14} erg cm^{-2} s^{-1} Å^{-1} in period 3, and that the linear relation seems to flatten for Hβ between 4 and 6×10^{-14} erg cm^{-2} s^{-1} in period 3. In the first period, there are only a few points for $Fc \leq 4 \times 10^{-14}$ erg cm^{-2} s^{-1} and they all correspond almost to the same value of Fc, but if one interpolates between these points and those at $Fc \sim 6 \times 10^{-14}$ erg cm^{-2} s^{-1},

Table 13. Time lags and CCF coefficients for the whole monitoring period, for the three periods based on the profile shapes, and for the division based on the three values of the continuum intensity.

Period	Hα	CCF	Hα-cent	Hβ	CCF	Hβ-cent
1996–2006	$5.70^{+27.05}_{-5.70}$	$0.87^{+0.02}_{-0.02}$	80.36 ± 12.93	$5.09^{+27.89}_{-5.09}$	$0.93^{+0.01}_{-0.01}$	69.79 ± 11.91
First	$0.68^{+3.30}_{-0.68}$	$0.67^{+0.09}_{-0.10}$	0.62 ± 1.11	$1.11^{+4.90}_{-1.11}$	$0.82^{+0.04}_{-0.05}$	11.61 ± 2.87
Second	$21.86^{+9.03}_{-10.53}$	$0.78^{+0.11}_{-0.14}$	66.07 ± 9.95	$11.15^{+5.00}_{-4.17}$	$0.88^{+0.06}_{-0.07}$	8.15 ± 2.38
Third	$0.81^{+1.55}_{-0.81}$	$0.94^{+0.02}_{-0.02}$	3.18 ± 1.76	$0.81^{+2.19}_{-0.81}$	$0.86^{+0.03}_{-0.04}$	16.17 ± 3.14
Continuum	Hα	CCF	Hα-cent	Hβ	CCF	Hβ-cent
$F^1_{\rm con}$	$0.27^{+0.73}_{-0.27}$	$0.51^{+0.22}_{-0.27}$	–	$25.15^{+13.77}_{-20.16}$	$0.50^{+0.23}_{-0.28}$	–
$F^2_{\rm con}$	$19.36^{+10.42}_{-5.44}$	$0.66^{+0.14}_{-0.17}$	0.56 ± 6.245	$0.62^{+3.49}_{-0.62}$	$0.70^{+0.07}_{-0.08}$	2.71 ± 5.22
$F^3_{\rm con}$	$1.19^{+6.01}_{-1.19}$	$0.67^{+0.07}_{-0.08}$	13.65 ± 4.47	$0.70^{+2.94}_{-0.70}$	$0.82^{+0.04}_{-0.04}$	12.28 ± 5.26

about the same relation is obtained as in periods 2 and 3. Still in the first period, when the continuum flux was more intense, i.e. $Fc \geq 7 \times 10^{-14}$ erg cm^{-2} s^{-1} Å^{-1}, the linear relation between the line and continuum fluxes disappeared, and the line fluxes saturated at values $\sim 30 \times 10^{-12}$ erg cm^{-2} s^{-1} for Hα and $\sim 8 \times 10^{-12}$ erg cm^{-2} s^{-1} for Hβ (see Fig. 12). Note finally that, if one extrapolates the continuum flux to zero linearly in the third period, it seems that the line flux is still larger than zero, being on the order of 5×10^{-12} erg cm^{-2} s^{-1} for Hα. It thus appears that the relation between the line and the continuum is not linear in the whole continuum flux range (2 to 12×10^{-14} erg cm^{-2} s^{-1}), but it steepens at low fluxes and saturates at high fluxes. This could occur when the ionizing incident flux is intense, so the medium reprocesses the irradiating flux into continua (Balmer, Pashen...) and not into lines (cf. for instance Collin-Souffrin & Lasota 1988).

Let us try to roughly model the response of the lines to a given continuum flux. For the highest value of the continuum flux, one gets an optical luminosity $L_{\rm opt} = \lambda L_\lambda \sim 10^{43}$ erg s^{-1}. One can then compute the ionizing flux incident on the BLR, assuming it to be on the order of the optical flux, $F_{\rm ion} \sim L_{\rm opt}/(4\pi R^2)$, where R is the radius of the BLR (of course it is a very rough approximation, to be refined in a subsequent paper). Assuming an average energy of the ionizing photons $\langle h\nu_{\rm ion}\rangle$ equal to 2 Rydbergs, and using the grids of models computed with Cloudy published by Korista et al. (1997) for a typical AGN spectrum (AGN3 in their list), one finds (Fig. 13) the Hβ fluxes at Earth as a function of the density, for a covering factor equal to unity, R = 3 and 30 light days, and for two values of the column density. We have also used a minimum optical flux of 10^{42} erg s^{-1} to compare with the high flux. We see that the computed line flux is of the order of the observed one only for a large (30 light-days) BLR, and for the larger flux (we recall that the observed fluxes of the broad component of Hβ is (2.3–9.8) 10^{-12} erg cm^{-2} s^{-1}). Since we know that the BLR extends in a wide range of radii, it leads to strongly suspect that a non-photoionized region is contributing to the Balmer lines. Such a "mechanically heated" region was invoked by Dumont et al. (1998) to account for the strong intensities of the Balmer lines in NGC 5548. This region could be associated with the radio jet. Indeed the radio image of NGC 4151 reveals a 0.2-pc two-sided base to the well-known arc-second radio jet (Ulvestad et al. 2005)[2]. Thus the BLR would be made of two-components: the usual one, ionized by the radiation of the accretion disc and its

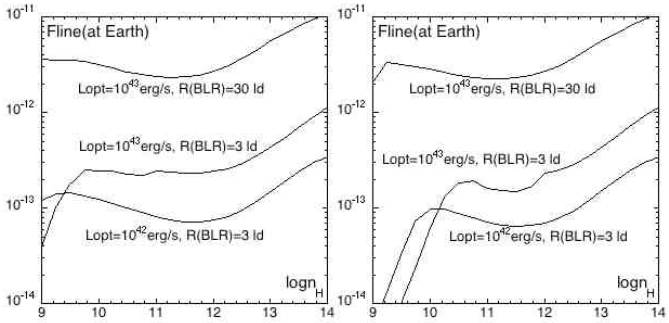

Fig. 13. Computed Hβ flux at Earth in erg cm^{-2} s^{-1} for the conditions of NGC 4151, as a function of the density in cm^{-3}; *left*, for a column density of 10^{24} cm^{-2}, *right* for 10^{23} cm^{-2}. See the text for more explanations.

corona, and another component, possibly associated with a rotating outflow surrounding the jet (Murray & Chiang 1997). In this second component, ionization and heating could be due either to relativistic particles or to a shock at the basis of the jet, and they could not be directly correlated to the ionizing continuum.

It is worthwhile recalling here the results obtained from the spectro-polarimetry of Hα by Martel (1998). He presented evidence that the scattering axes of different parts of the Hα profile correlate with the major morphological axes of the host galaxy of NGC 4151. If scattering is the dominant polarization mechanism in the BLR, then there are multiple lines of sight towards large-scale structures in the host galaxy, specifically the central bar, the radio jet, and the dynamical axis. Martel (1998) suggests that the line-emitting and scattering regions are cospatial, possibly in bulk flows moving along preferential axes defined by large-scale structures, such as streaming along the bar and inflow/outflow along the radio jet. In this case, the observed variability of the Hα profile and flux could be caused, at least partly, by dynamical effects, and not by a time-variable continuum source, as is usually assumed in reverberation mapping studies.

5. Conclusion

We have presented the results of a 11-year (1996–2006) spectral monitoring of the NGC 4151 nucleus. We have investigated the continuum and line variations during this period, and we reached the following conclusions:

(a) The nucleus of NGC 4151 showed big variations in the line and continuum fluxes during the monitoring period (1996–2006). The maximum of activity took place in 1996, and there were two minima between December 2000 and

[2] Note that Arshakian et al. (2006) found a correlation between the optical continuum and the radio-jet emission variability in the case of 3C 390.3.

May 2001 and between February 2005 and June 2005. The continuum flux changed by a factor ~6, the broad Hα and Hβ changed respectively by factors ~3.6 and ~5. The Hα, Hγ, and Heλ4686 fluxes were well-correlated with the Hβ flux (Fig. 9).

(b) There was a good linear relationship between the emission line and continuum flux variations when the continuum flux Fc was $\lesssim 7 \times 10^{-14}$ erg cm^{-2} s^{-1} Å^{-1}. When Fc was large ($Fc \gtrsim 7 \times 10^{-14}$ erg cm^{-2} s^{-1} Å^{-1}), the line fluxes either were weakly correlated or simply did not correlate at all with the continuum flux (Figs. 10 and 12).

(c) In the minimum state, the line wings were very weak and were only observed in Hβ and Hα. Thus the spectral type of the object in the monitoring period (1996−2000) changed from Sy1.8 during the minimum of activity to Sy1.5 during the maximum (Fig. 1).

(d) The flux ratios of the blue/red wings and blue (or red) wings/core varied differently for Hα and Hβ (Fig. 4). We found three characteristic periods (1996−1999, 2000−2001, and 2002−2006) in the profile variability. The behavior of the rms profiles in the three periods indicates that the BLR has a complex structure.

(e) From the CCF analysis, we found that the time lags were very uncertain. Since the CCF is often asymmetric, it implies that the line emitting gas extends in a wide range of radii, from 1 to 50 light days. But the correlation between continuum and line flux is strongest at lowest continuum flux levels, so the CCFs are defined best during these periods, i.e. in particular during periods 2 and 3. During these periods, the size of the BLR was relatively small (≤20 light-days). At high flux periods the CCFs are less well-defined, so it is very difficult to determine any lag.

(f) The lines and the continuum variations behave differently during the three periods. In the first period, when the continuum was strong, the line fluxes saturate, meaning that the optical continuum was not proportional to the ionizing continuum (Fig. 12). More generally, we found an excess of line emission with respect to a pure photoionization model during the whole monitoring period. This result could imply either the presence of a non-radiatively heated region or more ionizing to optical flux ratio than expected for a typical AGN spectrum.

A discussion of the line profiles and of the structure of the BLR will be given in a fortcoming paper (Paper II).

Acknowledgements. This work was supported by the INTAS (grant N96-0328), RFBR (grants N97-02-17625 N00-02-16272, N03-02-17123, and 06-02-16843), State program "Astronomy" (Russia), CONACYT research grant 39560-F and 54480 (México), and the Ministry of Science of the Republic of Serbia through the project Astrophysical Spectroscopy of Extragalactic Objects (146002). L.Č.P. is supported by the Alexander von Humboldt foundation through the Fritz Thyssen Special Programme. We would like to thank Tal Alexander for useful discussions concerning the time lags, and the referee Ian McHardy, for his comments and suggestions which contributed greatly to improving the paper.

References

Alexander, T. 1997, Astronomical Time Series, ed. D. Maoz, A. Sternberg, & E. M. Leibowitz (Dordrecht: Kluwer), 163
Antonucci, R. R. J., & Cohen, R. D. 1983, ApJ, 271, 564
Arshakian, T. G., et al. 2006 [arXiv:astro-ph/0602016]
Bentz, M. C., Denney, K. D., Cackett, E. M., et al. 2006, ApJ, 651, 775
Bochkarev, N. G., Zhekov, S. A., & Shapovalova, A. I. 1988, Adv. Space Res., 8, 625
Bochkarev, N. G., Shapovalova, A. I., & Zhekov, S. A. 1991, AJ, 102, 1278
Clavel, J., Boksenberg, A., Bromage, G. E., et al. 1990, MNRAS, 246, 668
Collin-Souffrin, S., & Lasota, J.-P. 1988, PASP, 100, 1041
Dumont, A. M., Collin-Souffrin, S., & Nazarova, L. 1998, A&A, 331, 11
Edelson, R. A., & Krolik, J. H. 1988, ApJ, 333, 646
Evans, I. N., Tsvetanov, Z., Kriss, G. A., et al. 1993, ApJ, 417, 82
Gaskell, C. M., & Sparke, L. S. 1986, ApJ, 305, 175
Gaskell, C. M., & Peterson, B. M. 1987, ApJS, 65, 1
Kaspi, S., Maoz, D., Netzer, H., et al. 1996, ApJ, 470, 336
Korista, K., Baldwin, J., Ferland, G., & Verner, D. 1997, ApJS, 108, 401
Lyuty, V. M. 2005, Pis'ma Astron. Zh., 31, 723 (Russian)
Malkov, Yu. F., Pronik, V. I., & Sergeev, S. G. 1997, A&A, 324, 904
Maoz, D., Netzer, H., Mazeh, T., et al. 1991, ApJ, 367, 493
Martel, A. R. 1998, ApJ, 508, 657
Metzroth, K. G., Onken, C. A., & Peterson, B. M. 2006, ApJ, 647, 901
Murray, N., & Chiang, G. 1997, ApJ, 474, 91
Nazarova, L. S., Gondhalekar, P. M., Bochkarev, N. G., & Shapovalova, A. I. 1998, A&A, 331, 471
Oknyanskij, V. L., Lyuty, V. M., Taranova, O. G., & Shenavrin, V. I. 1999, Astron. Lett., 25, 483
Penston, M. V., & Perez, E. 1984, MNRAS, 211, 581
Peterson, B. M. 1988, PASP, 100, 18
Peterson, B. M. 1993, PASP, 105, 207
Peterson, B. M., Pogge, R. W., Wanders, I., Smith, S. M., & Romanishin, W. 1995, PASP, 107, 579
Peterson, B. M., & Cota, S. A. 1988, ApJ, 330, 111
Sergeev, S. G., Pronik, V. I., & Sergeeva, E. A. 2001, ApJ, 554, 245
Shapovalova, A. I., Burenkov, A. N., & Bochkarev, N. G. 1996, Bull. Spec. Astrophys. Obs., 41, 28
Shapovalova, A. I., Doroshenko, V. T., Bochkarev, N. G., et al. 2004, A&A, 422, 925
Ulrich, M.-H. 2000, A&A Rev., 10, 135
Ulrich, M.-H., & Horne, K. 1996, MNRAS, 283, 748
Ulrich, M.-H., Boksenberg, A., Bromage, G. E., et al. 1984, MNRAS, 206, 221
Ulvestad, J. S., Wong, D. S., Taylor, G. B., Gallimore, J. F., & Mundell, C. G. 2005, AJ, 130, 936
Yaqoob, T., Warwick, R. S., Makino, F., et al. 1993, MNRAS, 262, 435
Van Groningen, E., & Wanders, I. 1992, PASP, 104, 700
Vlasyuk, V. V. 1993, Bull. Special Astrophys. Obs., 36, 107

Table 2. Log of the spectroscopic observations: Columns: 3 – code according to Table 1; 4 – projected spectrograph entrance apertures; 5 – wavelength range covered; 6 – spectral resolution; 7 – slit position angle (PA) in degrees; 8 – mean seeing in arcsec.

UT-date	JD (2 400 000+)	Code	Aperture (arcsec)	Sp. range (Å–Å)	Res. (Å)	PA (deg)	Seeing (″)
Jan. 11, 1996	+50 094.5	L1(G)	4.0 × 12.4	3840–5600	8	33	3
Jan. 15, 1996	+50 097.6	L1(G)	4.0 × 13.8	3640–7140	10	77	3
Jan. 16, 1996	+50 098.6	L1(G)	4.0 × 15	3640–7140	10	90	4.5
Feb. 14, 1996	+50 128.0	L(N)	1.5 × 6.0	3400–5440	10	211	2.4
Mar. 19, 1996	+50 162.4	L(N)	2.0 × 6.0	3650–5540	9	235	4.8
Mar. 20, 1996	+50 163.3	L(N)	2.0 × 6.0	4750–7340	13		3.5
Mar. 21, 1996	+50 164.4	L(N)	2.0 × 6.0	3650–5540	8	40	1.6
Mar. 22, 1996	+50 165.4	L1(G)	4.0 × 19.8	5700–7500	8		4
Mar. 23, 1996	+50 166.3	L(N)	2.0 × 6.0	4750–7340	13		
Apr. 26, 1996	+50 200.3	L(U)	2.0 × 6.0	4440–5200	5	353	2.4
Apr. 27, 1996	+50 201.3	L(U)	2.0 × 6.0	4440–5200	5	351	1.6
Jun. 14, 1996	+50 249.3	L(U)	2.0 × 6.0	4440–5240	5	131	2.4
Jul. 10, 1996	+50 275.3	L(U)	2.0 × 6.0	3700–5340	10	97	1.2
Jul. 11, 1996	+50 276.3	L(U)	2.0 × 6.0	6140–6950	6	131	1.4
Jul. 12, 1996	+50 277.3	L(U)	2.0 × 6.0	4450–5250	5	117	1.6
Jul. 15, 1996	+50 280.3	L(U)	2.0 × 6.0	4450–5250	5	123	1.6
Jul. 16, 1996	+50 281.3	L(U)	2.0 × 6.0	6140–6950	6		1.3
Nov. 05, 1996	+50 392.6	L(U)	2.0 × 6.0	4450–5250	5	27	3.2
Nov. 15, 1996	+50 402.6	L(U)	2.0 × 6.0	3700–5400	11	349	2
Mar. 02, 1997	+50 510.4	L(U)	2.0 × 6.0	4390–5200	5	333	2.4
Mar. 03, 1997	+50 511.4	L(U)	2.0 × 6.0	4440–5250	5	9	2.4
Apr. 05, 1997	+50 543.6	L1(G)	4.2 × 19.8	4140–5850	8	90	4.4
Apr. 06, 1997	+50 544.4	L1(G)	4.2 × 19.8	4140–5800	8	90	4.4
Apr. 08, 1997	+50 547.3	L(U)	2.0 × 6.0	4640–5450	5	353	3.2
Apr. 13, 1997	+50 552.3	L(U)	2.0 × 6.0	4440–5250	5	337	2
Dec. 27, 1997	+50 809.7	L(U)	2.0 × 6.0	4540–5340	5	153	1.6
Dec. 28, 1997	+50 810.7	L(U)	2.0 × 6.0	3840–7240	15	149	4
Jan. 20, 1998	+50 833.6	L(N)	2.0 × 6.0	3840–6150	8	141	1.2
Jan. 21, 1998	+50 834.6	L(N)	2.0 × 6.0	3840–6150	8	142	1.2
Jan. 23, 1998	+50 836.7	L(N)	2.0 × 6.0	4240–5500	5	131	1.2
Jan. 23, 1998	+50 836.7	L(N)	2.0 × 6.0	3840–6150	8	130	1.2
Jan. 28, 1998	+50 842.4	L(U)	2.0 × 6.0	4540–5350	5	357	1.6
Feb. 22, 1998	+50 867.4	L(N)	2.0 × 6.0	3840–6150	8	352	1.2
Apr. 30, 1998	+50 934.5	L1(G)	8.0 × 19.8	4100–5750	8	147	4.4
May 04, 1998	+50 938.3	L(N)	2.0 × 6.0	3740–6150	8	140	2.8
May 07, 1998	+50 940.5	L(N)	2.0 × 6.0	3740–6150	8	90	3.6
May 08, 1998	+50 941.5	L(N)	2.0 × 6.0	3740–6150	8	92	2
May 08, 1998	+50 942.5	L(N)	2.0 × 6.0	3740–6150	8	119	1.6
May 08, 1998	+50 942.5	L(N)	2.0 × 6.0	4140–5400	5	115	1.6
Jun. 20, 1998	+50 985.3	L1(G)	8.0 × 19.8	4120–5740	8	0	4.4
Jun. 26, 1998	+50 991.3	L(N)	2.0 × 6.0	3640–6040	8		2
Jul. 14, 1998	+51 008.7	GH	2.5 × 6.0	3970–7210	15	90	2
Jul. 16, 1998	+51 010.7	GH	2.5 × 6.0	3630–6890	15	90	2
Jul. 17, 1998	+51 011.6	GH	2.5 × 6.0	4210–7470	16	90	2
Jul. 21, 1998	+51 015.7	GH	2.5 × 6.0	4040–7280	12	90	2.7
Jul. 30, 1998	+51 025.3	L(U)	2.0 × 6.0	4540–5350	5	120	3.6
Nov. 13, 1998	+51 130.6	L1(G)	8.0 × 19.8	4140–5810	8	90	4.4
Dec. 19, 1998	+51 166.6	L1(G)	4.0 × 19.8	4140–5760	8	90	6.6
Jan. 12, 1999	+51 190.7	L(U)	2.0 × 6.0	6250–7100	9		2.5
Jan. 13, 1999	+51 191.9	GH	2.5 × 6.0	4140–7420	15	90	1.5
Jan. 14, 1999	+51 193.0	GH	2.5 × 6.0	4150–7430	15	90	1.3
Jan. 22, 1999	+51 200.5	L1(G)	4.2 × 19.8	4100–5740	8	90	2.2
Jan. 23, 1999	+51 201.6	L1(G)	4.2 × 19.8	4100–5740	8	0	4.4
Jan. 25, 1999	+51 203.6	L1(G)	4.2 × 19.8	4100–5750	9	0	6.6
Feb. 09, 1999	+51 218.6	L(U)	2.0 × 6.0	3640–8040	14	156	4
Feb. 12, 1999	+51 221.7	L(U)	2.0 × 6.0	3640–7940	14	156	1.6
Feb. 13, 1999	+51 222.6	L(U)	2.0 × 6.0	4290–5500	5	181	5.2
Feb. 14, 1999	+51 223.6	L(U)	3.0 × 6.0	4290–5500	5	143	2.4
Mar. 15, 1999	+51 252.9	GH	2.5 × 6.0	4200–7490	17	90	2.0
Mar. 20, 1999	+51 258.5	L1(G)	4.2 × 19.8	4090–5740	8	0	2.2
Mar. 23, 1999	+51 261.5	L1(G)	4.2 × 19.8	4090–5740	8	0	8.8
Mar. 24, 1999	+51 262.3	L1(G)	4.2 × 19.8	5590–7300	9		4
Mar. 24, 1999	+51 262.5	L(U)	2.0 × 6.0	4290–5450	5	62	4
Apr. 09, 1999	+51 277.6	L1(G)	4.2 × 19.8	4090–5750	8	0	4.4
Apr. 11, 1999	+51 279.5	L1(G)	4.2 × 19.8	4040–5740	8	0	6.6

Table 2. continued.

UT-date	JD (2 400 000+)	Code	Aperture (arcsec)	Sp.range (Å–Å)	Res. (Å)	PA (deg)	Seeing (″)
Apr. 15, 1999	+51 283.5	L1(G)	3.0 × 19.8	4090–5770	8	50	4.4
Jun. 14, 1999	+51 344.3	L1(G)	4.2 × 19.8	4090–5790	8	90	4.4
Jun. 16, 1999	+51 346.4	L1(G)	4.2 × 19.8	4090–5790	8	90	4.4
Dec. 02, 1999	+51 514.6	L1(G)	4.2 × 19.8	4090–5700	8	90	4.4
Dec. 03, 1999	+51 515.6	L1(G)	4.2 × 19.8	4140–5750	8	90	4.4
Dec. 05, 1999	+51 517.6	L1(G)	4.2 × 19.8	4090–5750	8	90	4.4
Jan. 09, 2000	+51 552.6	L1(G)	4.2 × 19.8	4090–5790	8	90	2.2
Jan. 10, 2000	+51 553.6	L1(G)	4.2 × 19.8	5640–7310	8	90	3.0
Jan. 27, 2000	+51 570.9	GH	2.5 × 6.0	4070–7340	13	90	3.0
Jan. 28, 2000	+51 571.9	GH	2.1 × 6.0	4070–7340	12	90	2.5
Feb. 11, 2000	+51 585.5	L1(G)	4.2 × 19.8	4040–5740	8	90	4.4
Feb. 14, 2000	+51 588.5	L1(G)	4.2 × 19.8	4040–5740	8	90	6.6
Feb. 14, 2000	+51 589.5	L1(G)	4.2 × 19.8	5590–7300	8	90	4
Feb. 26, 2000	+51 600.8	GH	2.1 × 6.0	4560–7590	12	90	2
Feb. 27, 2000	+51 601.8	GH	2.1 × 6.0	4300–7580	12	90	3
Apr. 03, 2000	+51 638.5	L1(G)	4.2 × 19.8	4090–5790	8	90	4.4
Apr. 05, 2000	+51 640.5	L1(G)	4.2 × 19.8	4040–5740	8	90	6.6
Apr. 25, 2000	+51 659.8	GH	2.1 × 6.0	4210–7490	12	90	2.5
Apr. 26, 2000	+51 660.8	GH	2.1 × 6.0	4210–7490	15	90	2.5
May 11, 2000	+51 676.4	L1(G)	4.2 × 19.8	4090–5790	10	90	4.4
May 25, 2000	+51 689.7	GH	2.5 × 6.0	4140–7390	15	90	2.5
May 26, 2000	+51 690.7	GH	2.5 × 6.0	4140–7390	15	90	3.5
Jul. 10, 2000	+51 736.4	L1(G)	4.2 × 19.8	4060–5750	8	90	6.6
Jul. 29, 2000	+51 755.3	L1(G)	4.2 × 19.8	4060–5750	8	90	4.4
Nov. 21, 2000	+51 869.6	L(U)	2.0 × 6.0	4242–5398	5	90	1.2
Nov. 30, 2000	+51 878.6	L1(G)	4.2 × 19.8	4090–5740	8	90	4.4
Dec. 17, 2000	+51 895.9	GH	2.5 × 6.0	4010–7310	13	90	2
Dec. 18, 2000	+51 897.0	GH	2.5 × 6.0	4010–7340	13	90	2
Dec. 19, 2000	+51 898.0	GH	2.5 × 6.0	4000–7270	15	90	4
Jan. 26, 2001	+51 936.5	L1(G)	4.2 × 19.8	5640–7300	8	90	2
Jan. 28, 2001	+51 937.5	L1(G)	4.2 × 19.8	4090–5750	8	90	4.4
Jan. 31, 2001	+51 940.6	L1(G)	4.2 × 19.8	4040–5700	8	90	4.4
Feb. 02, 2001	+51 943.5	L1(G)	4.2 × 19.8	4140–5750	8	90	6.6
Feb. 11, 2001	+51 952.4	L1(G)	4.2 × 19.8	4090–5750	8	0	4.4
Mar. 13, 2001	+51 981.7	GH	2.5 × 6.0	4130–7430	14	90	2
Apr. 13, 2001	+52 013.3	L1(G)	4.2 × 19.8	4090–5750	8	90	3.0
Apr. 16, 2001	+52 016.4	L1(G)	4.2 × 19.8	4090–5750	8	90	4.4
Apr. 29, 2001	+52 029.5	L1(G)	4.2 × 19.8	4090–5800	8	90	6.6
May 05, 2001	+52 034.6	GH	2.5 × 6.0	3600–6800	12	90	3.5
May 06, 2001	+52 036.4	L1(G)	4.2 × 19.8	4040–5750	8	90	4.4
May 12, 2001	+52 041.8	GH	2.5 × 6.0	3600–6880	15	90	1.5
May 14, 2001	+52 043.7	GH	2.5 × 6.0	4030–7340	13	90	2
Jun. 14, 2001	+52 074.7	GH	2.5 × 6.0	4020–7310	13	90	3.5
Jun. 15, 2001	+52 075.7	GH	2.5 × 6.0	4020–7310	17	90	2.5
Nov. 24, 2001	+52 237.6	L(U)	2.0 × 6.0	3640–6000	10	91	3.6
Nov. 24, 2001	+52 238.0	GH	2.5 × 6.0	4230–5900	8	90	2.5
Nov. 25, 2001	+52 239.0	GH	2.5 × 6.0	5680–7380	7.5	90	2.5
Jan. 23, 2002	+52 297.6	L1(G)	4.2 × 19.8	4040–5750	9	90	4.4
Jan. 24, 2002	+52 299.4	L1(G)	4.2 × 19.8	4040–5750	8	90	2.2
Feb. 21, 2002	+52 327.4	L1(G)	4.2 × 19.8	4040–5750	8	90	6.6
Feb. 22, 2002	+52 327.5	L(U)	2.0 × 6.0	3500–5840	9	90	3.2
Mar. 05, 2002	+52 338.7	GH	2.5 × 6.0	3900–7190	13	90	2
Mar. 06, 2002	+52 339.7	GH	2.5 × 6.0	5690–7390	7.5	90	2
Mar. 07, 2001	+52 340.8	GH	2.5 × 6.0	4260–5940	8	90	2
Mar. 17, 2002	+52 350.8	GH	2.5 × 6.0	4260–5940	8	90	3
Apr. 03, 2002	+52 367.7	GH	2.5 × 6.0	4280–5960	8	90	2
Apr. 04, 2002	+52 368.7	GH	2.5 × 6.0	5740–7440	7.5	90	2
Apr. 05, 2002	+52 369.7	GH	2.5 × 6.0	3820–7130	12	90	2
Apr. 06, 2002	+52 370.7	GH	2.5 × 6.0	3820–7130	12	90	1.5
May 03, 2002	+52 397.7	GH	2.5 × 6.0	4260–5940	8	90	2
May 04, 2002	+52 398.7	GH	2.5 × 6.0	5680–7370	7.5	90	2
May 05, 2002	+52 399.7	GH	2.5 × 6.0	4200–5880	8	90	2
May 16, 2002	+52 411.4	L1(G)	4.2 × 19.8	4090–5790	8	90	4.4
Jun. 02, 2002	+52 427.7	GH	2.5 × 6.0	4150–5820	8	90	2.5
Jun. 04, 2002	+52 429.7	GH	2.5 × 6.0	3990–7290	12	90	3.5
Jun. 05, 2002	+52 430.7	GH	2.5 × 6.0	4240–5920	7.5	90	3.0

Table 2. continued.

UT-date	JD (2 400 000+)	Code	Aperture (arcsec)	Sp.range (Å–Å)	Res. (Å)	PA (deg)	Seeing (″)
Jun. 24, 2002	+52 450.4	L(U)	2.0 × 6.0	3500–5880	8	90	2
Dec. 11, 2002	+52 620.0	GH	2.5 × 6.0	4230–6070	7.5	90	1.5
Dec. 12, 2002	+52 621.0	GH	2.5 × 6.0	5750–7430	8	90	1.8
Dec. 13, 2002	+52 622.0	GH	2.5 × 6.0	3740–7380	14	90	1.8
Dec. 14, 2002	+52 623.0	GH	2.5 × 6.0	4240–6080	8	90	1.8
Jan. 25, 2003	+52 665.0	GH	2.5 × 6.0	4300–5960	7.5	90	1.5
Jan. 26, 2003	+52 665.9	GH	2.5 × 6.0	5670–7360	7.5	90	4
Jan. 27, 2003	+52 666.9	GH	2.5 × 6.0	3920–7240	15	90	1.5
Jan. 28, 2003	+52 667.9	GH	2.5 × 6.0	3980–7300	12	90	2.5
Mar. 25, 2003	+52 723.8	GH	2.5 × 6.0	4240–6070	7.5	90	3.5
Mar. 26, 2003	+52 724.8	GH	2.5 × 6.0	3747–7385	12	90	4.5
Mar. 27, 2003	+52 725.8	GH	2.5 × 6.0	5600–7460	7.5	90	2.5
Apr. 10, 2003	+52 739.7	GH	2.5 × 6.0	5640–7500	8	90	4
Apr. 11, 2003	+52 740.8	GH	2.5 × 6.0	4130–5960	13	90	5.4
Apr. 12, 2003	+52 741.8	GH	2.5 × 6.0	3700–7340	12	90	4.0
Apr. 13, 2003	+52 743.3	L1(G)	4.2 × 19.8	5640–7330	9	90	2
May 08, 2003	+52 768.4	L1(U)	4 × 20.25	3750–6047	8	90	2.0
May 08, 2003	+52 768.3	L(U)	2.0 × 6.0	3690–6044	9	90	1.6
May 9, 2003	+52 769.3	L(U)	2.0 × 6.0	3690–6044	9	90	1.5
May 10, 2003	+52 770.3	L(U)	2.0 × 6.0	5740–8096	8	90	1.5
May 23, 2003	+52 782.7	GH	2.5 × 6.0	3540–7188	12	90	3.1
May 24, 2003	+52 783.8	GH	2.5 × 6.0	4240–6070	7.5	90	3.5
May 25, 2003	+52 784.7	GH	2.5 × 6.0	5582–7450	8	90	3.7
May 26, 2003	+52 785.7	GH	2.5 × 6.0	4230–6075	7.5	90	2.7
Jun. 22, 2003	+52 812.8	GH	2.5 × 6.0	4270–6970	7.5	90	1.8
Jun. 23, 2003	+52 813.7	GH	2.5 × 6.0	5620–7330	7.5	90	1.8
Nov. 22, 2003	+52 965.6	L1(G)	4.2 × 19.8	4089–5798	9	90	2.0
Nov. 23, 2003	+52 966.6	L1(G)	4.2 × 19.8	4090–5748	9	90	1.5
Nov. 24, 2003	+52 967.9	L1(G)	4.2 × 19.8	4090–5748	9	90	1.5
Dec. 22, 2003	+52 995.6	L1(U)	4.0 × 20.2	3750–6950	10	90	3.5
Jan. 28, 2004	+53 032.9	GH	2.5 × 6.0	4238–5950	12	90	2
Feb. 17, 2004	+53 053.0	GH	2.5 × 6.0	3736–7120	17	90	1.6
Mar. 17, 2004	+53 081.8	GH	2.5 × 6.0	4205–5920	12	90	2
Mar. 18, 2004	+53 082.7	GH	2.5 × 6.0	5664–7400	14	90	
Apr. 12, 2004	+53 107.6	Z2K	4.0 × 9.45	3784–7170	7.5	90	4.0
Apr. 13, 2004	+53 108.7	GH	2.5 × 6.0	4216–5930	12	90	2.5
Apr. 14, 2004	+53 109.7	GH	2.5 × 6.0	5622–7320	14	90	
May 20, 2004	+53 145.7	GH	2.5 × 6.0	4193–5910	12	90	2.22
May 21, 2004	+53 146.7	GH	2.5 × 6.0	5664–7390	7.5	90	
Jun. 12, 2004	+53 168.7	GH	2.5 × 6.0	4208–5920	10	90	2.73
Jun. 13, 2004	+53 169.7	GH	2.5 × 6.0	5592–7320	8	90	
Jun. 17, 2004	+53 173.7	GH	2.5 × 6.0	4213–5920	11	90	2.50
Dec. 15, 2004	+53 355.0	GH	2.5 × 6.0	4185–5870	7.5	90	2.96
Dec. 16, 2004	+53 356.0	GH	2.5 × 6.0	5739–7440	7.5	90	
Dec. 18, 2004	+53 357.6	L(S)	1.0 × 6.0	3900–7537	12.	270	1.6
Dec. 22, 2004	+53 361.5	L(S)	1.0 × 6.0	3900–7537	14	270	2.5
Jan. 16, 2005	+53 386.9	GH	2.5 × 6.0	3707–7096	12	90	3.05
Jan. 17, 2005	+53 388.0	GH	2.5 × 6.0	4183–5900	9	90	2.4
Jan. 18, 2005	+53 388.9	GH	2.5 × 6.0	5577–7320	12	90	
Feb. 07, 2005	+53 408.8	S-P	2.5 × 6.0	5722–7590	6.5	90	2.3
Feb. 15, 2005	+53 416.9	S-P	2.5 × 6.0	3708–5807	7	90	2.5
Feb. 15, 2005	+53 417.5	L1(U)	4.0 × 9.45	3750–7400	8	90	4.0
Mar. 17, 2005	+53 446.8	GH	2.5 × 6.0	5557–7300	13	90	
Mar. 18, 2005	+53 447.8	GH	2.5 × 6.0	3689–7090	13	90	3.0
Mar. 21, 2005	+53 451.3	L1(U)	4.0 × 9.45	3750–7400	9	90	8
Apr. 13, 2005	+53 474.4	L1(U)	4.0 × 9.45	3750–7400	8	90	2.5
Apr. 15, 2005	+53 475.8	GH	2.5 × 6.0	4245–5960	9	90	2.82
Apr. 16, 2005	+53 476.8	GH	2.5 × 6.0	5521–7256	10	90	
Apr. 16, 2005	+53 477.3	L1(U)	4.0 × 9.45	3750–7400	8	90	5.5
Apr. 18, 2005	+53 478.7	GH	2.5 × 6.0	3745–7190	13	90	
May 12, 2005	+53 503.3	L1(U)	4.0 × 9.45	3750–7400	8	90	2.0
May 13, 2005	+53 503.7	GH	2.5 × 6.0	4216–5910	9	90	3.0
May 14, 2005	+53 504.7	GH	2.5 × 6.0	5583–7300	7	90	
May 16, 2005	+53 507.4	L1(U)	4.0 × 9.45	3750–7400	8	90	3.2
Jun. 09, 2005	+53 530.7	GH	2.5 × 6.0	3714–7070	12	90	1.94
Jun. 10, 2005	+53 531.6	GH	2.5 × 6.0	4274–5970	9	90	3.37

Table 2. continued.

UT-date	JD (2 400 000+)	Code	Aperture (arcsec)	Sp.range (Å–Å)	Res. (Å)	PA (deg)	Seeing (″)
Jun. 11, 2005	+53 531.6	GH	2.5×6.0	5676–7395	7.5	90	
Jun. 16, 2005	+53 538.3	L1(U)	4.0×9.45	3740–7350	9	90	2.5
Nov. 28, 2005	+53 703.0	GH	2.5×6.0	3590–6900	15	90	3.0
Nov. 29, 2005	+53 704.0	GH	2.5×6.0	4230–5910	7	90	2.8
Dec. 06, 2005	+53 711.0	S-P	2.5×6.0	3690–5780	7	90	2.5
Dec. 07, 2005	+53 712.0	S-P	2.5×6.0	3690–5780	7	90	2.5
Dec. 27, 2005	+53 732.0	GH	2.5×6.0	3890–7270	17	90	3
Dec. 28, 2005	+53 733.0	GH	2.5×6.0	3880–7260	17	90	2.4
Jan. 21, 2006	+53 756.9	GH	2.5×6.0	4330–6040	9	90	2.7
Jan. 22, 2006	+53 757.9	GH	2.5×6.0	4330–6040	9	90	3
Jan. 24, 2006	+53 760.5	L1(U)	4.0×9.45	3740–7400	9	90	3.5
Jan. 25, 2006	+53 761.5	L1(U)	4.0×9.45	3740–7400	9	90	2.5
Feb. 20, 2006	+53 786.9	GH	2.5×6.0	3740–7120	17	90	2.8
Feb. 21, 2006	+53 787.5	L1(U)	4.0×9.45	3740–7400	8	90	2
Feb. 22, 2006	+53 788.5	L1(U)	4.0×9.45	3740–7400	8	90	2
Feb. 23, 2006	+53 789.5	GH	2.5×6.0	3740–7400	15	90	2.5
Mar. 09, 2006	+53 803.8	GH	2.5×6.0	3730–7100	14	90	5.1
Mar. 21, 2006	+53 816.4	L1(U)	4.0×9.45	3740–7400	8	90	5
Mar. 22, 2006	+53 817.4	L1(U)	4.0×9.45	3740–7400	8	90	4
Apr. 18, 2006	+53 843.7	GH	2.5×6.0	3720–7090	9	90	2.7
Apr. 19, 2006	+53 844.8	GH	2.5×6.0	4240–5940	7	90	2.5
Apr. 20, 2006	+53 845.7	GH	2.5×6.0	4240–5940	7	90	2.1
Apr. 20, 2006	+53 846.4	L1(U)	4.0×9.45	3740–7400	8	90	2.5

Table 3. Corrections for the position angle effect. Columns: 1 – position angle (PA) in degrees; 2 – projected spectrograph entrance apertures in arcsec; 3 – slit position angle (PA) corrections for emission lines (kp); 4 – estimated PA correction error for emission line, e(kp); 5 – position angle (PA) corrections for continuum flux, kp(cnt); 6 – the estimated PA correction error for continuum flux, e (kp(cnt)).

PA deg.	Aperture arcsec	kp(Hβ)	$\pm e$	kp(cnt)	$\pm e$
90	2.0×6.0	1		1	
90	4.0×20.4	1		1	
0	2.0×6.0	0.969	0.035	0.968	0.017
0	4.0×20.4	1.011	0.018	1.019	0.009
45	2.0×6.0	1.062	0.006	1.098	0.024
45	4×20.4	1.048	0.003	1.071	0.006
135	2.0×6.0	0.954	0.018	0.943	0.011
135	4.0×20.4	0.974	0.004	0.981	0.005

Table 4. Correction for seeing effects, for apertures $2''\times6''$ and $2.5''\times6''$. Columns: 1 – seeing intervals in arcsec; 2 – mean seeing in arcsec; 3 – our seeing correction for the emission lines fluxes, ks(our); 4 – estimated seeing correction error, $e(ks)$; 5 – Peterson's seeing correction for the emission lines fluxes from Peterson et al. (1995), ks(Pet); 6 – our host galaxy seeing correction for the continuum fluxes, in units of 10^{-14} erg s^{-1} cm^{-2} Å^{-1}, Gs(our); 7 – estimated host galaxy seeing correction error, $e(Gs)$; 8 – Peterson's host galaxy seeing correction Gs(Pet) for the continuum fluxes from Peterson et al. (1995).

Interval seeings arcsec	Mean seeing arcsec	ks(our) ($2''\times6''$) Hβ wings	±e	ks(Pet) ($2''\times10''$) Hβ	Gs(our) ($2''\times6''$) 10^{-14}	$\pm e$	Gs(Pet) ($2''\times10''$) 10^{-14}
1″–1.5″	1.25″	0.965	0.046		–0.160	0.197	–0.070 (1.3″)
	1.5″	0.977*		0.973			
1.5″–2.5″	2.0″	1.000		1.000	0		0
2.5″–3.5″	3.0″	1.042	0.030	1.052	–0.039		0.130
3.5″–4.5″	4.0″	1.069	0.063	1.086			
3.5″–5.2″					0.329	0.203	
	5″	1.096		1.105			0.31

Table 5. Corrections for the seeing effects, for aperture $4.2''\times19.8''$. Columns: 1 – Seeing intervals in arcsec; 2 – mean seeing in arcsec; 3 – our seeing correction for the emission lines fluxes, ks(our); 4 – the estimated seeing correction error, $e(ks)$; 5 – Peterson's seeing correction ks(Pet) for the emission lines fluxes from Peterson et al. (1995), ks(Pet); 6 – our host galaxy seeing correction for the continuum fluxes, in units of 10^{-14} erg s^{-1} cm^{-2} Å^{-1}), Gs(our); 7 – the estimated host galaxy seeing correction error, $e(Gs)$; 8 – Peterson's host galaxy seeing correction Gs(Pet) for the continuum fluxes from Peterson et al. (1995).

Interval seeings arcsec	Mean seeing arcsec	ks(our) Hβ ($4.2''\times19.8''$)	$\pm e$	ks(Pet) Hβ ($5''\times7.5''$)	Gs(our) 10^{-14} ($4.2''\times19.8''$)	$\pm e$	Gs(Pet) 10^{-14} ($2''\times10''$)
2″–4″	3″	1.000		1.000	0.000		0.000
4″–6″	5″	1.063	±0.022	1.004	0.031	±0.232	0.123
4″–8″	6″	1.080	±0.035	1.015	0.188	±0.292	
6″–8″	7″	1.116					
					0.503		0.245

Table 7. Observed continuum, Hα, Hβ, Hγ, and HeIIλ4686 fluxes, reduced to the 6 m telescope aperture $2'' \times 6''$. The fluxes are corrected for position angle (to PA = 90 degree), seeing, and aperture effects. Columns: 2 – the continuum flux at 5117 Å (in units of 10^{-14} erg s^{-1} cm^{-2} Å^{-1}), and the estimated continuum flux error; 3 – the Hα total flux and the Hα flux error; 4 – the Hβ total flux and the Hβ flux error; 5 – the Hγ total flux and the Hγ flux error; 6 – the HeIIλ4686 total flux and the HeIIλ4686 flux error. All line fluxes are in units of 10^{-12} erg s^{-1} cm^{-2}.

JD	F(cont) $\pm\ \varepsilon_{\rm cont}$	F(Hα) $\pm\ \varepsilon_{\rm H\alpha}$	F(Hβ) $\pm\ \varepsilon_{\rm H\beta}$	F(Hγ) $\pm\ \varepsilon_{\rm H\gamma}$	F(HeII) $\pm\ \varepsilon_{\rm HeII}$
50 094.5	8.8 ± 0.34	–	8.03 ± 0.31	4.807 ± 0.361	3.136 ± 0.031
50 097.6	9.26 ± 0.36	33.41 ± 0.63	8.19 ± 0.32	3.893 ± 0.292	2.707 ± 0.027
50 098.6	9.26 ± 0.36:	35.16 ± 0.63	–	–	–
50 128	11.25 ± 0.44	34.34 ± 0.65	9.28 ± 0.36	4.524 ± 0.339	3.495 ± 0.035
50 162.4	11.66 ± 0.45	–	8.9 ±0.35	3.638 ± 0.273	2.22 ± 0.022
50 163.3	11.66 ± 0.45:	33.79 ± 0.64	–	–	–
50 164.4	10.78 ± 0.42	–	8.5 ±0.33	4.044 ± 0.303	3.485 ± 0.035
50 165.4	10.78 ± 0.42:	33.24 ± 0.63	–	–	–
50 166.3	10.78 ± 0.42:	32.04 ± 0.61	–	–	–
50 200.3	9.6 ± 0.37	–	9.34 ± 0.36	–	–
50 201.3	8.85 ± 0.35	30.97 ± 0.59	8.73 ± 0.34	–	–
50 249.3	12.64 ± 0.49	35.45 ± 0.67	8.24 ± 0.32	–	–
50 275.3	11.99 ± 0.47	35.72 ± 0.68	9.83 ± 0.38	4.649 ± 0.349	3.313 ± 0.033
50 276.3	11.99 ± 0.47:	35.88 ± 0.68	–	–	–
50 277.3	11.29 ± 0.44	36.6 ± 0.70	9.26 ± 0.36	–	–
50 280.3	12.19 ± 0.48	35.95 ± 0.68	10 ±0.39	–	–
50 281.3	12.19 ± 0.48:	35.53 ± 0.68	–	–	–
50 392.6	10.04 ± 0.39	–	9.97 ± 0.39	–	–
50 402.6	10.65 ± 0.42	39.95 ± 0.76	10.8 ± 0.42	5.003 ± 0.375	3.792 ± 0.038
50 510.4	7.84 ± 0.41	32.4 ± 0.81	9.08 ± 0.15	–	–
50 511.4	8.86 ± 0.46	–	9.57 ± 0.15	–	–
50 543.6	6.82 ± 0.35	32.15 ± 0.80	7.44 ± 0.12	3.336 ± 0.200	2.088 ± 0.021
50 544.4	6.47 ± 0.34	32.54 ± 0.81	7.35 ± 0.12	–	–
50 547.3	6.92 ± 0.36	–	7 ± 0.11	–	–
50 552.3	7.38 ± 0.38	–	8.5 ± 0.14	–	–
50 809.7	7.56 ± 0.39	–	9.07 ± 0.15	–	–
50 810.7	7.22 ± 0.38	–	9.04 ± 0.14	–	–
50 833.6	5.91 ± 0.13	31.65 ± 0.98	7.31 ± 0.14	3.256 ± 0.189	1.912 ± 0.019
50 834.6	6.09 ± 0.13	31.03 ± 0.96	7.54 ± 0.14	3.466 ± 0.201	2.12 ± 0.021
50 836.7	6.4 ± 0.14	–	7.33 ± 0.14	3.837 ± 0.223	2.745 ± 0.027
50 836.7	6.42 ± 0.14	–	7.82 ± 0.15	3.619 ± 0.210	2.524 ± 0.025
50 842.4	6.59 ± 0.14	32.87 ± 1.02	8.02 ± 0.15	–	–
50 867.4	6.22 ± 0.14	33.34 ± 1.03	7.34 ± 0.14	3.363 ± 0.195	2.445 ± 0.024
50 934.5	6.39 ± 0.14	33.14 ± 1.03	7.06 ± 0.13	–	–
50 938.3	6.55 ± 0.14	33.6 ± 1.04	6.77 ± 0.13	2.643 ± 0.153	1.902 ± 0.019
50 940.5	6.27 ± 0.14	30.78 ± 0.95	6.82 ± 0.13	2.878 ± 0.167	1.457 ± 0.015
50 941.5	5.64 ± 0.12	–	6.41 ± 0.12	2.608 ± 0.151	1.135 ± 0.011
50 942.5	5.7 ± 0.13	29.87 ± 0.93	6.42 ± 0.12	2.432 ± 0.141	1.516 ± 0.015
50 942.5	6.09 ± 0.13	–	6.25 ± 0.12	2.653 ± 0.154	1.157 ± 0.012
50 985.3	8.52 ± 0.19	34.03 ± 1.05	8.29 ± 0.16	3.118 ± 0.181	2.738 ± 0.027
50 991.3	7.43 ± 0.16	–	8.24 ± 0.16	3.692 ± 0.214	2.946 ± 0.029
51 008.7	5.84 ± 0.13	31.09 ± 0.96	7.44 ± 0.14	3.355 ± 0.195	1.743 ± 0.017
51 010.7	5.98 ± 0.13	28.62 ± 0.89	7.59 ± 0.14	3.677 ± 0.213	2.173 ± 0.022
51 011.6	5.81 ± 0.13	28.82 ± 0.89	7.47 ± 0.14	3.258 ± 0.189	1.974 ± 0.020
51 015.7	6.26 ± 0.14	31.15 ± 0.97	7.84 ± 0.15	3.637 ± 0.211	1.829 ± 0.018
51 025.3	6.21 ± 0.14	30.15 ± 0.93	7.45 ± 0.14	–	–
51 130.6	5.69 ± 0.13	32.59 ± 1.01	7.05 ± 0.13	–	–
51 166.6	4.26 ± 0.09	33.07 ± 1.03	6.96 ± 0.13	–	–
51 190.7	5.56 ± 0.18:	29.56 ± 0.53	–	–	–
51 191.9	5.56 ± 0.18	28.47 ± 0.51	6.85 ± 0.16	3.54 ± 0.202	2.377 ± 0.150
51 193	5.81 ± 0.19	28.47 ± 0.51	6.6 ± 0.15	3.465 ± 0.198	2.62 ± 0.165
51 200.5	6.07 ± 0.19	–	7.36 ± 0.17	–	–
51 201.6	6.42 ± 0.21	33.51 ± 0.60	7.91 ± 0.18	–	–
51 203.6	6.57 ± 0.21	34.83 ± 0.63	8.05 ± 0.19	–	–
51 218.6	6.43 ± 0.21	35.24 ± 0.63	7.86 ± 0.18	3.74 ± 0.213	2.888 ± 0.182
51 221.7	6.38 ± 0.20	36.73 ± 0.66	8.09 ± 0.19	3.452 ± 0.197	3.043 ± 0.192
51 222.6	6.06 ± 0.19	–	7.92 ± 0.18	–	–
51 223.6	5.69 ± 0.18	–	7.34 ± 0.17	–	–
51 252.9	5.03 ± 0.16	29.45 ± 0.53	6.16 ± 0.14	2.886 ± 0.165	1.883 ± 0.119
51 258.5	5.79 ± 0.19	32.55 ± 0.59	6.95 ± 0.16	–	–
51 261.5	5.81 ± 0.19	31.19 ± 0.56	6.93 ± 0.16	–	–
51 262.3	5.77 ± 0.18:	31.47 ± 0.57	–	–	–
51 262.5	5.77 ± 0.18	32.2 ± 0.58	7.12 ± 0.16	–	–
51 277.6	5.79 ± 0.19	–	7.6 ± 0.17	3.425 ± 0.195	3.217 ± 0.203

Table 7. continued.

JD	F(cont) $\pm\ \varepsilon_{\rm cont}$	F(Hα) $\pm\ \varepsilon_{\rm H\alpha}$	F(Hβ) $\pm\ \varepsilon_{\rm H\beta}$	F(Hγ) $\pm\ \varepsilon_{\rm H\gamma}$	F(HeII) $\pm\ \varepsilon_{\rm HeII}$
51 279.5	5.5 ± 0.18	34.91 ± 0.63	7.51 ± 0.17	–	–
51 283.5	5.29 ± 0.17	–	6.56 ± 0.15	–	–
51 344.3	2.87 ± 0.09	–	4.2 ±0.10	1.716 ± 0.098	0.998 ± 0.063
51 346.4	2.75 ± 0.09	–	4.29 ± 0.10	2.212 ± 0.126	1.092 ± 0.069
51 514.6	2.77 ± 0.09	–	3.52 ± 0.08	1.668 ± 0.095	1.252 ± 0.079
51 515.6	2.79 ± 0.09	22.94 ± 0.41	3.6 ±0.08	1.58 ± 0.090	1.193 ± 0.075
51 517.6	3.1 ± 0.10	–	3.47 ± 0.08	1.574 ± 0.090	1.391 ± 0.088
51 552.6	4.16 ± 0.10	–	4.51 ± 0.09	–	–
51 553.6	4.16 ± 0.10:	25.93 ± 0.93	–	–	–
51 570.9	3.86 ± 0.09:	25.13 ± 0.90	–	–	–
51 571.9	3.86 ± 0.09	23.57 ± 0.85	4.67 ± 0.10	2.257 ± 0.065	1.035 ± 0.049
51 585.5	3.56 ± 0.08	–	4.16 ± 0.09	2.615 ± 0.076	1.52 ± 0.071
51 588.5	3.6 ± 0.08	–	4.48 ± 0.09	2.021 ± 0.059	1.517 ± 0.071
51 589.5	3.6 ± 0.08:	24.12 ± 0.87	–	–	–
51 600.8	2.78 ± 0.06	22.51 ± 0.81	4.01 ± 0.08	–	–
51 601.8	2.77 ± 0.06	22.28 ± 0.80	4.15 ± 0.09	–	–
51 638.5	2.53 ± 0.06	–	3.7 ± 0.08	–	–
51 640.5	2.3 ± 0.05	–	3.57 ± 0.07	–	–
51 659.8	2.63 ± 0.06	20.19 ± 0.73	3.6 ± 0.08	1.88 ± 0.055	1.156 ± 0.054
51 660.8	2.61 ± 0.06	19.04 ± 0.69	3.56 ± 0.07	1.943 ± 0.056	1.144 ± 0.054
51 676.4	1.88 ± 0.04	–	3.23 ± 0.07	–	–
51 689.7	1.95 ± 0.04	17.89 ± 0.64	3.09 ± 0.06	1.678 ± 0.049	0.649 ± 0.031
51 690.7	1.92 ± 0.04	19.68 ± 0.71	3.01 ± 0.06	1.528 ± 0.044	0.711 ± 0.033
51 736.4	2.31 ± 0.05	–	3.22 ± 0.07	–	–
51 755.3	2.72 ± 0.06	–	3.35 ± 0.07	–	–
51 869.6	1.86 ± 0.04	–	3.84 ± 0.08	2.061 ± 0.060	0.844 ± 0.040
51 878.6	1.51 ± 0.03	–	3.14 ± 0.07	1.687 ± 0.049	0.918 ± 0.043
51 895.9	1.7 ± 0.04	15.92 ± 0.57	2.49 ± 0.05	1.203 ± 0.035	0.71 ± 0.033
51 897	1.7 ± 0.04	16.61 ± 0.60	2.55 ± 0.05	1.18 ± 0.034	0.698 ± 0.033
51 898	1.79 ± 0.04	16.22 ± 0.58	2.64 ± 0.06	1.2 ± 0.035	0.806 ± 0.038
51 936.5	1.79 ± 0.07:	20.81 ± 0.60	–	–	–
51 937.5	1.79 ± 0.07	–	2.96 ± 0.05	–	–
51 940.6	1.81 ± 0.07	18.73 ± 0.54	2.91 ± 0.05	–	–
51 943.5	1.76 ± 0.07	20.09 ± 0.58	2.94 ± 0.05	–	–
51 952.4	1.31 ± 0.05	–	2.75 ± 0.04	–	–
51 981.7	1.71 ± 0.06	14.31 ± 0.41	2.32 ± 0.04	1.11 ± 0.047	0.625 ± 0.008
52 013.3	2.24 ± 0.09	15.86 ± 0.46	2.47 ± 0.04	–	–
52 016.4	2.6 ± 0.10	17.27 ± 0.50	2.63 ± 0.04	–	–
52 029.5	1.78 ± 0.07	–	2.79 ± 0.04	–	–
52 034.6	1.8 ± 0.07	12.97 ± 0.38	2.46 ± 0.04	1.127 ± 0.047	0.684 ± 0.009
52 036.4	1.93 ± 0.07	–	2.61 ± 0.04	1.217 ± 0.051	0.86 ± 0.011
52 041.8	1.83 ± 0.07	13.31 ± 0.39	2.26 ± 0.04	1.107 ± 0.046	0.696 ± 0.009
52 043.7	1.99 ± 0.08	13.71 ± 0.40	2.25 ± 0.04	1.155 ± 0.049	0.608 ± 0.008
52 074.7	2.68 ± 0.10	17.38 ± 0.50	3.41 ± 0.05	1.667 ± 0.070	0.687 ± 0.009
52 075.7	2.84 ± 0.11	15.08 ± 0.44	3.13 ± 0.05	1.539 ± 0.065	0.798 ± 0.010
52 237.6	3.34 ± 0.13	21.66 ± 0.63	5.06 ± 0.08	2.221 ± 0.093	1.432 ± 0.019
52 238	3.33 ± 0.13	–	5.12 ± 0.08	–	–
52 239	3.33 ± 0.13:	20.55 ± 0.60	–	–	–
52 297.6	3.45 ± 0.07	–	4.23 ± 0.16	–	–
52 299.4	3.68 ± 0.08	19.87 ± 0.54	3.95 ± 0.15	–	–
52 327.4	3.21 ± 0.07	–	3.86 ± 0.15	–	–
52 327.5	3.14 ± 0.07	–	3.89 ± 0.15	1.35 ± 0.073	0.988 ± 0.055
52 338.7	4.17 ± 0.09	19.93 ± 0.54	3.99 ± 0.16	1.773 ± 0.096	1.378 ± 0.077
52 339.7	4.17 ± 0.09:	21.14 ± 0.57	–	–	–
52 340.8	3.96 ± 0.08	–	4.42 ± 0.17	–	–
52 350.8	2.74 ± 0.06	–	4.03 ± 0.16	1.666 ± 0.090	0.755 ± 0.042
52 367.7	3.94 ± 0.08	–	3.83 ± 0.15	–	–
52 368.7	3.94 ± 0.08:	19.06 ± 0.51	–	–	–
52 369.7	3.79 ± 0.08	19.39 ± 0.52	3.73 ± 0.15	1.605 ± 0.087	0.863 ± 0.048
52 370.7	3.91 ± 0.08	19.29 ± 0.52	3.93 ± 0.15	1.671 ± 0.090	0.911 ± 0.051
52 397.7	3.3 ± 0.07	–	3.89 ± 0.15	1.368 ± 0.074	0.622 ± 0.035
52 398.7	3.3 ± 0.07:	18.82 ± 0.51	–	–	–
52 399.7	3.27 ± 0.07	–	3.72 ± 0.15	1.347 ± 0.073	0.568 ± 0.032
52 411.4	3.84 ± 0.08	–	4.04 ± 0.16	–	–
52 427.7	3.72 ± 0.08	–	4 ± 0.17	1.447 ± 0.078	0.693 ± 0.039
52 429.7	3.71 ± 0.08	20.55 ± 0.55	4.34 ± 0.17	1.718 ± 0.093	0.762 ± 0.043
52 430.7	3.75 ± 0.08	–	4.04 ± 0.16	–	–

Table 7. continued.

JD	F(cont) $\pm\ \varepsilon_{\rm cont}$	F(Hα) $\pm\ \varepsilon_{\rm H\alpha}$	F(Hβ) $\pm\ \varepsilon_{\rm H\beta}$	F(Hγ) $\pm\ \varepsilon_{\rm H\gamma}$	F(HeII) $\pm\ \varepsilon_{\rm HeII}$
52 450.4	4.24 ± 0.09	21.93 ± 0.59	4.5 ±0.18	1.571 ± 0.085	1.325 ± 0.074
52 620	3.36 ± 0.07	–	4.29 ± 0.17	–	–
52 621	3.36 ± 0.07:	19.15 ± 0.52	–	–	–
52 622	3.44 ± 0.07	19.95 ± 0.54	4.32 ± 0.17	1.914 ± 0.103	0.769 ± 0.043
52 623	3.58 ± 0.08	–	4.76 ± 0.19	–	–
52 665	5.07 ± 0.17	–	4.79 ± 0.14	–	–
52 665.9	5.07 ± 0.17:	24.08 ± 0.67	–	–	–
52 666.9	5.07 ± 0.17	22.26 ± 0.62	4.79 ± 0.14	2.027 ± 0.097	1.21 ± 0.092
52 667.9	5.57 ± 0.18	23.24 ± 0.65	4.96 ± 0.14	2.246 ± 0.108	1.364 ± 0.104
52 723.8	4.54 ± 0.15	–	5.35 ± 0.16	2.304 ± 0.111	1.227 ± 0.093
52 724.8	4.17 ± 0.14	22.59 ± 0.63	4.96 ± 0.14	2.277 ± 0.109	1.369 ± 0.104
52 725.8	4.17 ± 0.14:	21.54 ± 0.60	–	–	–
52 739.7	5.17 ± 0.17:	23.31 ± 0.65	–	–	–
52 740.8	5.17 ± 0.17	–	5.97 ± 0.17	2.729 ± 0.131	1.347 ± 0.102
52 741.8	5.15 ± 0.17	23.5 ± 0.66	5.36 ± 0.16	2.603 ± 0.125	1.65 ± 0.125
52 743.3	5.15 ± 0.17:	22.47 ± 0.63	–	–	–
52 768.4	5.16 ± 0.17	–	5.67 ± 0.16	–	–
52 768.3	5.08 ± 0.17	–	5.44 ± 0.16	2.173 ± 0.104	1.277 ± 0.097
52 769.3	5.33 ± 0.18	24.39 ± 0.68	5.57 ± 0.16	2.064 ± 0.099	1.353 ± 0.103
52 770.3	5.33 ± 0.18:	23.29 ± 0.65	–	–	–
52 782.7	5.03 ± 0.17	24.98 ± 0.70	5.82 ± 0.17	2.488 ± 0.119	1.387 ± 0.105
52 783.8	5.17 ± 0.17	–	5.47 ± 0.16	2.714 ± 0.130	1.374 ± 0.104
52 784.7	5.55 ± 0.17:	23.56 ± 0.66	–	–	–
52 785.7	5.55 ± 0.18	–	5.31 ± 0.15	–	–
52 812.8	4.18 ± 0.14	–	5.74 ± 0.17	2.467 ± 0.118	1.429 ± 0.109
52 813.7	4.18 ± 0.14:	22.76 ± 0.64	–	–	–
52 965.6	3.68 ± 0.12	–	4.79 ± 0.14	–	–
52 966.6	3.46 ± 0.11	–	4.87 ± 0.14	2.428 ± 0.117	1.371 ± 0.104
52 967.9	3.3 ± 0.11	–	4.83 ± 0.14	2.709 ± 0.130	1.588 ± 0.121
52 995.6	3.52 ± 0.12	–	5.55 ± 0.16	2.504 ± 0.120	2.258 ± 0.172
53 032.9	3.26 ± 0.09	–	4.38 ± 0.10	2.111 ± 0.082	0.849 ± 0.062
53 053	3.19 ± 0.09	20.35 ± 0.53	4.92 ± 0.11	2.405 ± 0.094	1.4 ± 0.102
53 081.8	2.76 ± 0.08	–	4.18 ± 0.10	1.861 ± 0.073	0.695 ± 0.051
53 082.7	2.76 ± 0.08:	17.91 ± 0.47	–	–	–
53 107.6	2.03 ± 0.06:	16.54 ± 0.43	–	–	–
53 108.7	2.03 ± 0.06	–	3.04 ± 0.70	1.432 ± 0.056	0.452 ± 0.033
53 109.7	2.03 ± 0.06:	16.14 ± 0.42	–	–	–
53 145.7	1.92 ± 0.05	–	2.64 ± 0.06	1.18 ± 0.046	0.585 ± 0.043
53 146.7	1.92 ± 0.05:	14.7 ± 0.38	–	–	–
53 168.7	2.29 ± 0.07	–	2.74 ± 0.06	1.088 ± 0.042	0.601± 0.044
53 169.7	2.29 ± 0.07:	14.21 ± 0.37	–	–	–
53 173.7	2.7 ± 0.08	–	2.76 ± 0.06	1.338 ± 0.052	0.607 ± 0.044
53 355	2.85 ± 0.08	–	3.72 ± 0.09	1.618 ± 0.063	0.857 ± 0.061
53 356	2.85 ± 0.08:	18.13 ± 0.47	–	–	–
53 357.6	2.85 ± 0.08	18.91 ± 0.49	3.71 ± 0.09	1.466 ± 0.057	0.799 ± 0.058
53 361.5	2.81 ± 0.08	17.85 ± 0.46	3.48 ± 0.08	1.481 ± 0.058	0.616 ± 0.045
53 386.9	2.56 ± 0.06	19.21 ± 0.52	3.84 ± 0.08	1.736 ± 0.057	0.756 ± 0.056
53 388	2.57 ± 0.06	–	3.79 ± 0.08	1.692 ± 0.056	0.625 ± 0.046
53 388.9	2.57 ± 0.06:	17.64 ± 0.48	–	–	–
53 408.8	2.3 ± 0.06:	16.94 ± 0.46	–	–	–
53 416.9	2.04 ± 0.05	–	2.96 ± 0.06	1.294 ± 0.043	0.639 ± 0.047
53 417.5	2.04 ± 0.05:	16.36 ± 0.44	–	–	–
53 446.8	1.92 ± 0.05:	16.16 ± 0.44	–	–	–
53 447.8	1.92 ± 0.05	16.62 ± 0.45	3.07 ± 0.06	1.376 ± 0.045	0.716 ± 0.053
53 451.3	2.14 ± 0.05	16.8 ± 0.45	3.1 ± 0.06	–	–
53 474.4	1.73 ± 0.05:	14.01 ± 0.38	–	–	–
53 475.8	1.73 ± 0.04	–	2.47 ± 0.05	1.014 ± 0.033	0.62 ± 0.046
53 476.8	1.73 ± 0.04:	13.97 ± 0.38	–	–	–
53 477.3	1.78 ± 0.04:	15.77 ± 0.43	–	–	–
53 478.7	1.83 ± 0.04	15.08 ± 0.41	2.42 ± 0.05	1.071 ± 0.035	0.684 ± 0.051
53 503.3	2.16 ± 0.05	14.79 ± 0.40	2.51 ± 0.05	–	–
53 503.7	2.16 ± 0.05	–	2.74 ± 0.05	1.241 ± 0.041	0.796 ± 0.059
53 504.7	2.16 ± 0.05:	14.65 ± 0.40	–	–	–
53 507.4	2.1 ± 0.05	15.76 ± 0.43	2.6 ± 0.05	–	–
53 530.7	1.89 ± 0.05	15.07 ± 0.41	2.62 ± 0.05	1.168 ± 0.039	0.681 ± 0.050
53 531.6	1.94 ± 0.05	–	2.74 ± 0.05	–	–
53 531.6	1.94 ± 0.05:	14.92 ± 0.40	–	–	–

Table 7. continued.

JD	F(cont) $\pm$ $\varepsilon_{\rm cont}$	F(Hα) $\pm$ $\varepsilon_{\rm H\alpha}$	F(Hβ) $\pm$ $\varepsilon_{\rm H\beta}$	F(Hγ) $\pm$ $\varepsilon_{\rm H\gamma}$	F(HeII) $\pm$ $\varepsilon_{\rm HeII}$
53 538.3	1.74 ± 0.04	13.25 ± 0.36	2.49 ± 0.05	1.207 ± 0.040	0.93 ± 0.069
53 703	3.73 ± 0.09	18.92 ± 0.51	4.42 ± 0.09	–	–
53 704	3.57 ± 0.09	–	4.44 ± 0.09	1.577 ± 0.052	1.357 ± 0.100
53 711	3.04 ± 0.07	–	4.3 ±0.09	2.071 ± 0.068	1.036 ± 0.077
53 712	2.79 ± 0.07	–	4.32 ± 0.09	2.197 ± 0.073	1.01 ± 0.075
53 732	2.41 ± 0.06	15.84 ± 0.43	3.49 ± 0.07	1.733 ± 0.057	0.904 ± 0.067
53 733	2.45 ± 0.06	16.01 ± 0.43	3.39 ± 0.07	–	–
53 756.9	1.88 ± 0.05	–	3.14 ± 0.05	–	–
53 757.9	1.92 ± 0.05	–	3.16 ± 0.05	–	–
53 760.5	1.8 ± 0.04	15.62 ± 0.33	2.81 ± 0.04	–	–
53 761.5	1.82 ± 0.04	16.59 ± 0.35	2.89 ± 0.05	1.372 ± 0.091	0.845 ± 0.073
53 786.9	2.07 ± 0.05	15.64 ± 0.33	3.16 ± 0.05	1.69 ± 0.112	0.767 ± 0.066
53 787.5	1.91 ± 0.05	16.57 ± 0.35	3.31 ± 0.05	1.775 ± 0.117	0.982 ± 0.084
53 788.5	1.94 ± 0.05	16.39 ± 0.34	3.31 ± 0.05	1.544 ± 0.102	0.876 ± 0.075
53 789.5	1.94 ± 0.05:	16.55 ± 0.35	–	1.724 ± 0.114	1.027 ± 0.088
53 803.8	3.25 ± 0.08	16.9 ± 0.35	3.43 ± 0.05	1.684 ± 0.111	1.087 ± 0.093
53 816.4	3.22 ± 0.08	17.83 ± 0.37	3.98 ± 0.06	1.843 ± 0.122	1.471 ± 0.127
53 817.4	3.06 ± 0.07	17.79 ± 0.37	4.04 ± 0.06	1.755 ± 0.116	1.571 ± 0.135
53 843.7	3.53 ± 0.08	19.68 ± 0.41	4.55 ± 0.07	2.34 ± 0.154	1.407 ± 0.121
53 844.8	3.41 ± 0.08	–	4.52 ± 0.07	2.071 ± 0.137	1.458 ± 0.125
53 845.7	3.32 ± 0.08	–	4.38 ± 0.07	2.054 ± 0.136	1.58 ± 0.136
53 846.4	3.31 ± 0.08	19.01 ± 0.40	4.6 ±0.07	2.083 ± 0.137	1.887 ± 0.162

Table 8. Mean error (uncertainty) of our flux determinations for continuum, Hα, Hβ, Hγ, and HeII 4686 emission lines in different years, and in the whole (11 years) observation period. Columns: 2 and 3 – the estimated mean continuum flux error in % and its sigma; 4 and 5 – the estimated mean Hα flux error in % and its sigma; 6 and 7 – the estimated mean Hβ flux error in % and its sigma; 8 and 9 – the estimated mean Hγ flux error in % and its sigma; 10 and 11 – the estimated mean flux error in % and its sigma, Bottom – mean error (uncertainty) in the whole (11 years) observation period.

Year	ε_c	$\pm\sigma$	$\varepsilon_{H\alpha}$	$\pm\sigma$	$\varepsilon_{H\beta}$	$\pm\sigma$	$\varepsilon_{H\gamma}$	$\pm\sigma$	ε_{HeII}	$\pm\sigma$
1996	3.9	2.27	1.9	1.2	3.90	1.56	7.5		10.4	4.20
1997	5.17	2.98	2.19	1.63	1.63	1.81	6.0	1.62	10.22	4.20
1998	2.18	1.37	3.1	2.4	1.90	1.42	5.75	1.62	10.18	4.70
1999	3.24	2.22	1.75	1.28	2.29	1.68	5.65	4.95	6.26	3.00
2000	2.3	3.65	3.62	2.31	2.12	0.82	2.88	2.53	4.65	4.47
2001	3.77	3.16	2.9	1.13	1.63	2.25	4.2	1.7	12.90	4.67
2002	2.05	1.38	2.7	1.66	3.91	2.44	5.37	5.9	5.60	1.56
2003	3.34	2.37	2.8	1.49	2.86	2.44	4.82	2.67	7.62	4.76
2004	2.65	2.26	2.6	0.8	2.25	3.18	3.85	4.45	7.28	4.57
2005	2.37	2.14	2.72	2.63	1.96	2.22	3.3	1.31	7.37	5.86
2006	2.42	1.76	2.12	1.68	1.62	1.34	6.58	1.97	8.62	4.71
mean (1996–2006)	2.84	1.23	2.46	0.75	2.37	0.84	4.99	1.46	7.78	2.51